Decoding the complexity of delayed wound healing following *Enterococcus faecalis* infection

Cenk CELIK[1,5], Stella Yue Ting LEE[1], Frederick Reinhart TANOTO[2], Mark VELEBA[2], Kimberly A. KLINE[1,2,3], Guillaume THIBAULT[1,4]

[1]School of Biological Sciences and [2]Singapore Centre for Environmental Life Science Engineering, Nanyang Technological University, Singapore

[3]Department of Microbiology and Molecular Medicine, Faculty of Medicine, University of Geneva, Switzerland

[4]Mechanobiology Institute, National University of Singapore, Singapore

[5]Present address: Department of Genetics, Evolution and Environment, Genetics Institute, University College London, London, UK

Correspondence to:

Kimberly Kline, Tel: +41 (0)22 379 56 02; email: Kimberly.Kline@unige.ch

Guillaume Thibault, Tel: +65 6592 1787; email: thibault@ntu.edu.sg

Running title: Infected wound single-cell atlas

ABSTRACT

Wound infections are highly prevalent, and can lead to delayed or failed healing, causing significant morbidity and adverse economic impacts. These infections occur in various contexts, including diabetic foot ulcers, burns, and surgical sites. *Enterococcus faecalis* is often found in persistent non-healing wounds, but its contribution to chronic wounds remains understudied. To address this, we employed single-cell RNA sequencing (scRNA-seq) on infected wounds in comparison to uninfected wounds in a mouse model. Examining over 23,000 cells, we created a comprehensive single-cell atlas that captures the cellular and transcriptomic landscape of these wounds. Our analysis revealed unique transcriptional and metabolic alterations in infected wounds, elucidating the distinct molecular changes associated with bacterial infection compared to the normal wound healing process. We identified dysregulated keratinocyte and fibroblast transcriptomes in response to infection, jointly contributing to an anti-inflammatory environment. Notably, *E. faecalis* infection prompted a premature, incomplete epithelial-to-mesenchymal transition in keratinocytes. Additionally, *E. faecalis* infection modulated M2-like macrophage polarization by inhibiting pro-inflammatory resolution *in vitro*, *in vivo,* and in our scRNA-seq atlas. Furthermore, we discovered macrophage crosstalk with neutrophils, which regulates chemokine signaling pathways, while promoting anti-inflammatory interactions with endothelial cells. Overall, our findings offer new insights into the immunosuppressive role of *E. faecalis* in wound infections.

INTRODUCTION

Infections pose a challenge to the wound healing process, affecting both the skin's protective barrier and the efficient repair mechanisms required for tissue integrity. The skin, the largest and most intricate defense system in mammals, exhibits unique cellular heterogeneity and complexity that maintain tissue homeostasis. Within the skin, undifferentiated resident cells are the main modulators of tissue maintenance, albeit terminal differentiation dynamics adapt to the regenerative requirements of the tissue. Several comprehensive studies conducted in mice and humans have highlighted the complexity of the skin (Cheng et al., 2018; Der et al., 2019; Joost et al., 2020; Joost et al., 2018; Joost et al., 2016; Philippeos et al., 2018; Theocharidis et al., 2022). However, these studies have primarily focused on cellular heterogeneity and the transcriptome of intact skin or uninfected wounds, offering limited insights into the dynamics of wound healing following infection.

Efficient healing during wound infections involves a sequence of events occurring in three distinct but interconnected stages: inflammation, proliferation, and remodeling (Eming et al., 2014; Masson-Meyers et al., 2020; Minutti et al., 2017; Rognoni & Watt, 2018). These events involve a series of inter- and intracellular molecular interactions mediated by soluble ligands and the innate immune system (Lindley et al., 2016; Wang et al., 2018). The inflammatory phase initiates migration of leukocytes into the wound site to help clear cell debris and establish tissue protection through local inflammation. Initially, neutrophils, responding to pro-inflammatory cytokines like IL-1β, TNF-α, and IFN-γ, extravasate through the endothelium to the site of injury. Subsequently, the proliferative stage aims to reduce wound size through contraction and re-establishment of the epithelial barrier. This stage is facilitated by activated keratinocytes modulated by inflammatory responses, cytokines, and growth factors. In the final stage, tissue remodeling restores the mechanical properties of intact skin through ECM reorganization, degradation, and synthesis (Wang et al., 2018). Dysregulation of this intricate mechanism can lead to pathological outcomes characterized by persistent inflammation and excessive ECM production (Ashcroft et al., 2013).

Enterococcus faecalis (*E. faecalis*) is a commensal bacterium in the human gut, and also an opportunistic pathogen responsible for various infections, including surgical site infections and diabetic ulcers (Kao & Kline, 2019). Bacterial wound infections in general, including those associated with *E.*

faecalis, are biofilm-associated, resulting in an antibiotic-tolerant population that may lead to persistent infections (Ch'ng et al., 2019). Additionally, *E. faecalis* has mechanisms to evade and suppress immune clearance by, for example, suppressing the pro-inflammatory M1-like phenotype in macrophage and preventing neutrophil extracellular trap formation (Kao et al., 2023; Kao & Kline, 2019; Tien et al., 2017). *E. faecalis* can also persist (Bertuccini et al., 2002; Gentry-Weeks et al., 1999; Horsley et al., 2018; Horsley et al., 2013; Olmsted et al., 1994; Wells et al., 1990; Wells et al., 1988; Zou & Shankar, 2014, 2016) and replicate (da Silva et al., 2022; Nunez et al., 2022) within epithelial cells and macrophages, further complicating treatment. The combination of biofilm formation and immune evasion makes Enterococcal wound infections a significant clinical challenge.

In a murine full-thickness excisional wound model, our prior investigations revealed a bifurcated trajectory characterizing *E. faecalis* wound infections (Chong et al., 2017). Initially, bacterial colony-forming units (CFU) increase in number in the acute replication phase, with a concomitant pro-inflammatory response characterized by pro-inflammatory cytokine and chemokine production coupled with neutrophil infiltration. In the subsequent persistence stage, *E. faecalis* CFU undergo gradual reduction and stabilization at approximately 10^5 CFU within wounds by 2-3-day post-infection (dpi), coinciding with delayed wound healing. Within this framework, we have identified specific bacterial determinants that contribute to each phase of *E. faecalis* infection. For example, *de novo* purine biosynthesis emerges as a pivotal factor in enhancing bacterial fitness during the acute replication phase (Tan et al., 2022). In the persistent phase at 3 dpi, the galactose and mannose uptake systems, in conjunction with the *mprF* gene product, are associated with nutrient acquisition and resistance to antimicrobial peptides and neutrophil-mediated killing, respectively (Bao et al., 2012; Chong et al., 2017; Jin et al., 2021; Kandaswamy et al., 2013; Rashid et al., 2023). Nonetheless, the intricate interplay between these *E. faecalis* persistence-associated virulence factors, their immunomodulatory evasion strategies, and precise implications in the context of delayed wound healing remains to be investigated.

To address this, we generated a comprehensive single-cell atlas of the host response to persistent *E. faecalis* wound infection. We observed that *E. faecalis* induces immunosuppression in keratinocytes and fibroblasts, delaying the immune response. Notably, *E. faecalis* infection prompted a partial epithelial-to-mesenchymal transition (EMT) in keratinocytes. Moreover, macrophages in infected

wounds displayed M2-like polarization. Our findings also indicate that the interactions between macrophages and endothelial cells contribute to the anti-inflammatory niche during infection. Furthermore, *E.* faecalis-infected macrophages drive pathogenic vascularization signatures in endothelial cells, resembling the tumor microenvironment in cancer. We also noted *E. faecalis* infected-associated macrophage crosstalk with neutrophils, regulating chemokine signaling pathways and promoting anti-inflammatory interactions with endothelial cells. These insights from our scRNA-seq atlas provide a foundation for future studies aimed at investigating bacterial factors contributing to wound pathogenesis and understanding the underlying mechanisms associated with delayed healing.

RESULTS

E. faecalis infection inhibits wound healing signatures

In the wound environment, various cell types, including myeloid cells, fibroblasts, and endothelial cells, play critical roles in the initial and later stages of wound healing by releasing platelet-derived growth factor (PDGF). Additionally, macrophages secrete epidermal growth factor (EGF) in injured skin, which operates through the epidermal growth factor receptor (EGFR) to promote keratinocyte proliferation, migration, and re-epithelialization. To understand the impact of *E. faecalis* infection on wound healing, we infected excisional dorsal wounds on C57BL/6J male mice and measured gene expression levels of wound healing markers in bulk tissue at 4 dpi at the onset of persistent infection. We then compared the expression profiles with those of (i) wounded but uninfected or (ii) unwounded and uninfected controls, ensuring that the uninfected and infected mice were of comparable weight (**Figures 1A**, **S1A**, and **S1B**). We observed lower expression of platelet-derived growth factor subunit A (*Pdgfa*) in *E. faecalis*-infected wounds than in unwounded skin, while uninfected wounds remained unchanged. Similarly, the expression of *Egf* was lower in uninfected wounds than in healthy skin, while reaching the lowest levels in *E. faecalis*-infected wounds. The reduced *Egf* expression in uninfected wounds at 4 days post-wounding is expected, as EGF primarily influences skin cell growth, proliferation, and differentiation during the later stages of wound healing, typically around 10 days post-injury (Schultz et al., 1991). By contrast, wounding alone resulted in higher transforming growth factor beta 1 (*Tgfb1*) expression. TGF-β1 plays a dual role in wound healing depending on the microenvironment. During tissue maintenance, TGF-β1 acts as a growth inhibitor, and its absence in the epidermis leads to keratinocyte hyperproliferation (Guasch et al., 2007). Elevated TGF-β1 levels have also been observed

in the epidermis of chronic wounds in both humans and mouse models (Li et al., 2021; Xie et al., 2009). In addition, we observed a slightly higher expression of fibroblast growth factor 1 (*Fgf1*) in uninfected wounds, although the differences were comparable (**Figure S1A**). Overall, the persistent *E. faecalis* infection contributed to higher *Tgfb1* expression, whilst *Pdgfa* levels remained low, correlating with delayed wound healing.

Single-cell transcriptomes of full-thickness skin wounds diverge during healing and infection

To understand the cellular heterogeneity in the wound environment following *E. faecalis* infection, we dissociated cells from full-thickness wounds, including minimal adjacent healthy skin. We generated single-cell transcriptome libraries using the droplet-based 10X Genomics Chromium microfluidic partitioning system (**Figure 1B** and **Table S1**). By integrating the transcriptomes of approximately 23,000 cells, we employed the unbiased graph-based Louvain algorithm to identify clusters (Zappia & Oshlack, 2018). Our analysis revealed 24 clusters, irrespective of infection (**Figure S1C**). These clusters included epithelial, immune, fibroblast, endothelial, vascular, and neural cell types (**Figures 1C**, **1D**, **S1D**, **S1E**, and **Tables S2-S4**). Within the epithelial class, we identified basal (BAS1-3) and suprabasal (SUP1-4) keratinocytes, hair follicles (HFSUP1-2), outer bulge (OB), and sebaceous gland (SG) cells (**Figure 1E**). The immune class included macrophages (MC1-2), neutrophils (NEUT1-2), memory T cells (TC), and a mixed population (DC/LC) of dendritic cells (DCs) and Langerhans cells (LC). Notably, cells from infected wounds (~13,000 cells) demonstrated distinct clustering patterns compared to cells from uninfected wounds (~9,500 cells) (**Figure S1F** and **Table S1**).

We proceeded to analyze upregulated gene signatures for each Louvain cluster (**Figure 1F** and **Table S2**) and compared them to the cell-type signature database (Franzen et al., 2019) (PanglaoDB) to identify characteristic gene expression patterns (**Figure 1G**). Additionally, we identified highly expressed genes in uninfected and infected wounds (**Tables S3** and **S4**) and performed co-expression network analysis (WGCNA) to uncover the core genes associated with cell types (**Figure 1H**).

We also delineated macrophage populations (**Figure S1G-I**), identifying an M2-like polarization (**Figure 1F**, MC1) marked by higher expression of *Arg1*, *Egr2*, *Fn1*, and *Fpr2* (**Figure S1G**), and a tissue-resident macrophage (TRM) population (**Figure 1F**, MC2) expressing *Ccr5*, *Cd68*, *Fcgr1*, *Mrc1*

(*Cd206*), *Ms4a4c*, and *Pparg* (**Figure S1H**). Both macrophage populations exhibited limited expression of *Grp18* and *Nos2* (*iNos*), which are typically associated with M1-like polarization (**Figure S1I**). Together, our analysis outlined the differences observed in uninfected and infected wound healing across epithelial, fibroblast, and immune cell populations.

E. faecalis **elicit immunosuppressive interactions with keratinocytes**

Keratinocytes, the predominant cell population in the skin, include undifferentiated (basal) and differentiated (suprabasal, hair follicle, outer bulge, and sebaceous gland) cells within the EPI cell class in both wound types (**Figure 1C**). Further analysis of the EPI class revealed 19 clusters (**Figure 2A** and **Table S5**), with the emergence of infection-specific clusters (**Figure 2B**, clusters 0 and 6, and **S2A**). We identified three major keratinocyte populations: (i) *Krt5*-expressing ($Krt5^{hi}$) basal keratinocytes, (ii) *Krt10*-enriched ($Krt10^{hi}$) post-mitotic keratinocytes, and (iii) $Krt5^{hi}Krt10^{hi}$ co-expressing populations (**Figure 2C**). The co-expression of *Krt5* and *Krt10* was unique to infection-specific clusters (**Figure 2A**, clusters 0 and 6). We also observed distinct populations, including hair follicle stem cells ($Lrg5^{hi}$; cluster 10), differentiating basal cells (Ivl^{hi}; clusters 7 and 8), terminally differentiated keratinocytes (Lor^{hi}; clusters 2, 8, 16, 17), and bulge stem cells ($Krt15^{hi}$; clusters 2, 9, 10, 17, 18) (**Figure 2D**), reflecting the skin's complexity.

The two largest infection-specific clusters exhibited distinct gene expression patterns, with cluster 0 and cluster 6, enriched in *Zeb2* and *Gjb6* expression, respectively (**Figure 2A**). These clusters represent migratory stem-like and partial EMT keratinocyte populations (**Figure 2E**). As the barrier to pathogens, keratinocytes secrete a broad range of cytokines that can induce inflammatory responses (Alshetaiwi et al., 2020; Siriwach et al., 2022; Veglia et al., 2021). However, $Zeb2^{hi}$ keratinocytes co-expressing *Cxcl2*, *Il1b,* and *Wfdc17*, indicate myeloid-derived suppressor cell-like phenotype which implies an immunosuppressive environment (Hofer et al., 2021; Veglia et al., 2021). Gene Ontology analysis revealed that the $Zeb2^{hi}$ and $Gjb6^{hi}$ clusters exhibited signatures related to ECM remodeling, chemokine signaling, migratory pathways, and inflammatory response (**Figures 2F**, **2G**, and **Table S5**). Collectively, these findings suggest an early migratory role of keratinocytes induced by *E. faecalis* infection.

During cutaneous wound healing, keratinocytes enter a mesenchymal-like state, migrating to and proliferating within the wound site. We observed two infection-specific keratinocyte populations enriched in *Zeb2* and *Gjb6* expression, respectively, as early as four days post-wounding. To determine the nature of these populations, we performed RNA velocity analysis, a method that predicts the future state of individual cells based on the patterns of temporal gene expression (La Manno et al., 2018). RNA velocity analysis predicted a lineage relationship between *Zeb2*^{hi} and *Gjb6*^{hi} keratinocytes (**Figures 2H**, **2I**, and **Table S5**). The top lineage-driver genes (Lange et al., 2022), including *Rgs1*, *H2-Aa*, *Ms4a6c*, *Cd74*, *H2-Eb1* and *H2-Ab1*, were predominantly expressed in the infection-specific cluster 0 (**Figures 2J** and **S2B**). These genes are associated with the major histocompatibility complex (MHC) class II, suggesting a self-antigen presenting keratinocyte population, which have a role in co-stimulation of T cell responses (Meister et al., 2015; Tamoutounour et al., 2019). Meanwhile, *Gjb6*^{hi} keratinocytes demonstrated reduced expression of putative genes such as *Pof1b*, *Krt77*, *Dnase1l3,* and *Krtdap* as well as increased *Clic4* expression (**Figure S2C**), suggesting that *E. faecalis* infection perturbs normal healing. Additionally, temporal expression analysis of high-likelihood genes revealed three distinct transcriptional states (**Figure 2K**): (1) an early state characterized by undifferentiated (basal) keratinocyte markers, (2) an intermediate state defined by the selection and upkeep of intraepithelial T cell protein family, and (3) a late state characterized by cell adhesion signatures. These findings provide insights into the cellular dynamics and developmental abnormalities, such as partial EMT induced by *E. faecalis* infection during wound healing.

Understanding cell-cell crosstalk through ligand-receptor interactions allows predicting ligand-target links between interacting cells by combining their expression data with signaling and gene regulatory network databases. Given our observation that infection-specific keratinocyte populations (**Figure S2**) were involved in ECM remodeling and immune response (**Figures 2F** and **2G**), we hypothesized that these cells might participate in the SPP1 signaling pathway. SPP1 (secreted phosphoprotein 1 or osteopontin) is a chemokine-like protein secreted by immune cells, osteoblasts, osteocytes, and epithelial cells to facilitate anti-apoptotic immune responses (Denhardt et al., 2001; Standal et al., 2004). To decipher ligand-receptor interactions in uninfected and infected skin wounds, we performed cell-cell interaction analysis (Guerrero-Juarez et al., 2019). We found 34 predicted interactions in uninfected keratinocytes and 61 in keratinocytes from *E. faecalis*-infected wounds out of a total of 923 and 991

interactions, respectively, in our single-cell atlas (**Figures S1A**, **S1B**, and **Table S6**). Importantly, we detected outgoing signals from keratinocytes to other cells associated with EGF and SPP1 signaling pathways. Ligand:receptor pairs in the infected niche (**Figure S2D**) included Hbegf:Egfr for the EGF pathway and Spp1:Cd44, Spp1:(Itga5+Itgb1), Spp1:(Itga9+Itgb1), and Spp1:(Itgav+Itgb3) for the SPP1 pathway (**Figures 2L**, **S2D**, and **S2E**), that are known to induce immunosuppression (Cheng et al., 2023; Gao et al., 2022). Remarkably, we observed the enrichment of keratinocyte-endothelial cell ligand:receptor pairs (**Figure S3** and **Table S6**). By contrast, keratinocytes from uninfected wounds only showed macrophage migration inhibitory factor (MIF) ligand interactions with its receptors Cd44, Cd74, and Cxcr4 in immune cells (DC/LC and TRM) (**Figure S2G**), suggesting that these keratinocytes promote cell proliferation, wound healing, and survival (Farr et al., 2020; Jager et al., 2020). Furthermore, the RNA velocity of keratinocytes from uninfected wounds revealed a terminal hair follicle (*Lrg5*^{hi}) and a proliferating keratinocyte (*Mki67*^{hi}) population originating from basal keratinocytes (**Figure 2H**), underlining normal wound healing. Overall, *E. faecalis* infection altered the transcriptome of keratinocytes towards a partial EMT at an early stage, whereas uninfected keratinocytes showed differentiating and terminally differentiated keratinocyte populations (**Figure 2M**). Our data show that epidermal cells undergo migratory and inflammatory gene regulation during normal wound healing (Haensel et al., 2020; Vu et al., 2022), whereas *E. faecalis* induces anti-inflammatory transcriptional modulation that may promote chronicity in bacteria-infected skin wounds. These findings demonstrate that keratinocytes exist in a low inflammation profile under homeostasis, which is exacerbated upon *E. faecalis* infection.

E. faecalis **delays immune response in fibroblasts**

Fibroblasts are the fundamental connective tissue cells involved in skin homeostasis and healing. Upon injury, they primarily (1) migrate into the wound site, (2) produce ECM by secreting growth factors, and (3) regulate the inflammatory response. Despite their high heterogeneity, fibroblast subpopulations have distinct roles in wound healing. In response to injury, fibroblasts produce increased amounts of ECM by inhibiting the metalloproteinase (MMP) family through the tissue inhibitor of metalloproteinases 1 (TIMP1). Notably, Guerrero-Juarez *et al.* (2019) reported a rare fibroblast population expressing myeloid lineage cell markers during normal (uninfected) wound healing (Guerrero-Juarez et al., 2019). Our bioinformatic analysis identified fibroblast populations within wounds that differed significantly

between infected and uninfected conditions (**Figure S1F**). Further analysis of the fibroblast mega class revealed 12 distinct clusters, with clusters 0 and 2 specific to infection while retaining their fibroblastic identity (**Figures 3A**, **3B**, and **Table S7**). The infection-associated fibroblasts express a range of markers, including those linked to extracellular matrix deposition such as *Col1a1*, *Col1a2*, *Col6a2*, vimentin (*Vim*), fibronectin, elastin (*Eln*), asporin (*Aspn*), platelet-derived growth factor receptor-beta (*Pdgfrb*), and fibroblast activator protein-α (*Fap*). These findings suggest a premature extracellular matrix deposition triggered by *E. faecalis*, which typically occurs in later stages of wound healing processes (Deng et al., 2021; Fang et al., 2023; Fitzgerald & Weiner, 2020) (**Figures 3C**, **3D**, **S4A**, and **S4B**).

The unique fibroblast clusters 0 and 2 associated with *E. faecalis* infection (**Figure 3E**) exhibited enrichment of myeloid-specific markers (*Hbb-bs*, *Lyz2*) and profibrotic gene signatures (*Inhba*, *Saa3*, *Timp1*) (**Table S6**). Additionally, *Lyz2*^{hi} fibroblasts co-expressing *Tagln*, *Acta2*, and *Col12a1* suggested their origin as contractile myofibroblasts (Guerrero-Juarez et al., 2019). Gene Ontology analysis indicated that *Lyz2*^{hi} fibroblasts were involved in immune response (**Figure 3F**), while *Timp1*^{hi} fibroblasts were associated with tissue repair processes (**Figure 3G**). These findings collectively reveal an intricate cellular landscape within infected wounds, highlighting the detrimental functional contributions of various fibroblast subpopulations in response to *E. faecalis* infection.

To validate the distinct fibroblast cell states and their differentiation potential, we performed RNA velocity analysis (**Figures 3H** and **3I**), which revealed two terminal fibroblast populations: (1) a *Cilp*^{hi} fibrotic cluster 4 and (2) an *Mkx*^{hi} reparative cluster 5, originating from clusters 0 and 2 (**Figure 3I** and **Table S7**), indicating the mesenchymal characteristics of infection-specific fibroblasts. Lineage driver gene analysis supported these findings, with the expression of genes such as *Csgalnact1*, *Atrnl1*, *Slit3*, *Rbms3*, and *Magi2*, which are known to induce fibrotic tissue formation under pathological conditions (Gornicki et al., 2022; Mizumoto et al., 2020) (**Figures 3J** and **S4C**). Similarly, the activation of genes such as *Serping1*, *Sparc*, *Pcsk5*, *Fgf7*, and *Cyp7b1* (**Figure S4D**) indicated the temporal activation of cell migration and immune suppression during infection. CellRank analysis revealed two states: an initial prolonged state and a short terminal state (**Figure 3K**). The early transcriptional states were associated with apoptosis inhibition, cell adhesion, and immune evasion genes, including serine

protease inhibitors (*Serpine1* and *Serping1*), *Prrx1*, *Ncam1*, and *Chl1*, suggesting immune suppression. By contrast, the terminal state showed the emergence of migratory (*Cd74*, *Ifi202b*) and inflammatory (*Acod1*, *Cxcl2*, *F13a1*, and *S100a9*) genes, indicating a delayed immune response to *E. faecalis* infection. Overall, these findings indicate that uninfected fibroblasts contribute to healthy wound healing with proliferative and elastin-rich fibroblast populations. By contrast, *E. faecalis*-infected fibroblasts exhibit a pathological repair profile, characterized by the presence of *Timp1*^{hi} and *Lyz2*^{hi} fibroblasts (**Figure 3L**).

To understand the role of fibroblast subpopulations in healing, we explored cell-cell interactions in fibroblasts in infected wound (**Figure S4E**). In *E. faecalis*-infected wounds, we observed interactions involving Spp1 ligand with cell adhesion receptor Cd44 and integrins (Itgav+Itgb1, Itgav+Itgb3, Itgav+Itgb5, Itga4+Itgb1, Itga5+Itgb1, Itga9+Itgb1), and EGF signaling pairing Ereg:Egfr (**Figures S4F** and **S4G**). These interactions were particularly strong between macrophages (ligands) and endothelial cells (receptors) (**Figure S2C**), suggesting their involvement in the infected wound microenvironment. By contrast, uninfected wounds showed a normal wound healing profile with reparative VEGF and TGF-β signaling pathways (**Figures S4H** and **S4I**). Furthermore, RNA velocity analysis of fibroblasts from uninfected wounds revealed two terminal fibroblast populations originating from *Fbn1*^{hi} fibroblasts: elastin-rich (*Eln*^{hi}) fibroblasts and keratinocyte-like (*Krt1*^{hi}/*Krt10*^{hi}) fibroblasts (**Figure 3H**). Collectively, our findings revealed the unique roles of fibroblasts upon *E. faecalis* infection and reaffirmed the known functions of fibroblasts during uninfected wound healing, consistent with the outcomes of predicted ligand-receptor interactions (**Figure 3F**).

E. faecalis **promotes macrophage polarization towards an anti-inflammatory phenotype**

Immune cells play a crucial role in wound healing by eliminating pathogens, promoting keratinocyte and fibroblast activity, and resolving inflammation and tissue repair (Haensel et al., 2020; Landen et al., 2016; Vu et al., 2022). Our data reveal unique clusters enriched within keratinocytes and fibroblasts in *E. faecalis*-infected wounds, suggesting an immunosuppressive transcriptional program in these cell populations (**Figures S2A** and **S4B**). Given the ability of *E. faecalis* to actively suppress macrophage activation *in vitro* (Tien et al., 2017), we investigated if *E. faecalis* contributes to anti-inflammatory macrophage polarization and immune suppression *in vivo*. Analysis of the myeloid cells identified two

infection-specific macrophage clusters (clusters 2 and 5) among 12 clusters (**Figures 4A**, **4B**, and **Table S8**). To validate infection-specific macrophage polarization, we performed qPCR on bulk tissue isolated from uninfected and infected wounds at 4 dpi. Infected wounds showed downregulation of *Mrc1* and upregulation of both *Arg1* and *Nos2* compared to uninfected wounds or unwounded bulk skin tissue (**Figure 4D**), which was further corroborated by examining gene expression in bone marrow-derived macrophages (BMDM) following *E. faecalis* infection *in vitro* (**Figure 4E**). The co-expression of both M1-like and M2-like macrophage markers during infection has been previously reported for *M. tuberculosis* (Mattila et al., 2013), *T. cruzi* (Cuervo et al., 2011), and *G. lamblia* infections (Maloney et al., 2015), as an indicator of an immunosuppressive phenotype that promotes an anti-inflammatory environment during prolonged infection. In myeloid clusters of our scRNA-seq atlas, tissue-resident macrophages (*Mrc1*) were predominant in uninfected wounds, while M2-like macrophages (*Arg1*) were abundant in macrophages from *E. faecalis*-infected wounds (**Figures 4F** and **4G**), supporting the hypothesis of an anti-inflammatory wound environment during *E. faecalis* infection. Additionally, our analysis allowed the segregation of dendritic cells and Langerhans cells (cluster 10, *Cd207* and *Itgax*) from macrophage populations, characterized by the co-expression of langerin (*Cd207*) and integrin alpha X (*Itgax*/*Cd11c*) in cluster 10 (**Figure 4G**), confirming the validity of our cell annotation.

Next, we focused on the functions of infection-specific macrophage clusters 2 and 5 (**Figures 4B** and **S5B**) to identify their potential roles in wound infection. Gene Ontology analysis revealed that these macrophages were involved in the immune response, ECM production, and protein translation (**Figures S5C** and **S5D**). To better understand the evolution of infection-specific macrophages, we computed the RNA velocity to explore potential lineage relationships (**Figures 4H** and **4I**). RNA velocity identified cluster 2 macrophages as the terminal population in the infected dataset (**Figure 4I**), whereas uninfected terminal macrophage populations were found as clusters 1 and 4 (**Figure 4H**). As expected, cluster 5 did not exhibit velocity vectors since these cells were highly segregated from the main myeloid clusters and differed vastly in their gene expression (**Table S8**). While both terminal macrophage populations in both uninfected and infection conditions co-host anti-inflammatory macrophage signatures, their transcriptional program and functions vary in the presence of *E. faecalis* infection.

To further characterize clusters 2 and 5, we explored differentially expressed genes in infected cells. We identified the inflammation-related genes *Fth1*, *Slpi*, *Il1b*, *AA467197* (*Nmes1*/miR-147), *Ptges,* and *Cxcl3* (**Figures 4J** and **S5E**), suggesting that these cells may play a role in tissue remodeling (Munadziroh et al., 2022; Recalcati et al., 2019). Similarly, the expression of the infected-specific top likelihood genes *Cxcl2*, *Cd36,* and *Pdpn* was associated with the presence of efferocytic M2-like macrophages (**Figure S5F**, green clusters). The distant *Sparc*^{hi} macrophage cluster 5 exhibited C-C chemokine receptor type 7 (*Ccr7*) exhaustion (**Figure S5F**, red clusters), indicating that these cells might be of M1-like origin (Hu et al., 2020).

Next, to validate whether the terminal macrophage populations corresponding to clusters 2 and 5 were tissue-resident or M2-like macrophages, we computed the driver genes of macrophage sub-clusters over latent time. The top 50 likelihood gene heat map identified two major states in the macrophages (**Figure 4K**). The early state cells were enriched in antigen-presenting/processing MHC class II gene expression such as *H2-Ab1*, *H2-Eb1, H2-Eb2,* G-protein-coupled receptors (*Gpr137b*, *Grp171,* and *Gpr183*), and mannose receptor c-type 1 (*Mrc1*/*Cd206*). In contrast, *Cd36*, *Met*, *Sgms2*, *Fn1*, *Zeb2,* and *Arg2* levels were higher in the late macrophage population, suggesting M2-like polarization. Therefore, we asked whether these macrophages provide an immunosuppressive microenvironment during *E. faecalis* infection. Cellular interactome analysis revealed enrichment of the ANNEXIN signaling pathway, particularly Anxa1:Fpr1 and Anxa1:Fpr2 ligand-receptor pairs between M2-like macrophage and endothelial or neutrophil cells (**Figure S5I-K**), which inhibits pro-inflammatory cytokine production (Yang et al., 2009). Together, these results demonstrate that *E. faecalis* infection influences macrophage polarization towards an anti-inflammatory phenotype. Importantly, the ANXA1:FPR1 interaction has been implicated in the tumor microenvironment of several malignancies (Cheng et al., 2014; Takaoka et al., 2018; Vecchi et al., 2018; Zhao et al., 2022), indicating that the *E. faecalis*-infected wound niche mimics the anti-inflammatory transcriptional program of the tumor microenvironment.

Neutrophils contribute to the anti-inflammatory microenvironment

Our findings revealed an exacerbated inflammatory phenotype during infection (**Figures 2F**, **2G**, **3K**, and **4J**), specifically marked by an abundance of neutrophils (Chong et al., 2017) (**Figure 1D**). To facilitate a comparison of the broader immune niche, we focused on the neutrophil population,

identifying six subpopulations in the integrated dataset (**Figure 5A** and **Table S9**). Among these, clusters 0 and 2 were abundant in the infected condition (**Figures 5B** and **S6A**). The expression of granulocyte colony-stimulating factor receptor (*Csf3r*) and integrin subunit alpha M (*Itgam*/*Cd11b*) was highly expressed across all neutrophils (**Figure 5C**). Furthermore, the higher expression of chemokine (CXC motif) receptor 2 (*Cxcr2*), Fc gamma receptor III (*Fcgr3*/*Cd16*), and ferritin heavy chain (*Fth1*) in clusters 0, 1, 2, 4 and 5 indicated the presence of migrating and maturing neutrophils, regardless of infection status (**Figure 5D**). By contrast, cluster 3 did not express *Cxcr2* and *Fcgr3* and had lower expression of *Fth1* but was enriched in calcium/calmodulin-dependent protein kinase type ID (*Camk1d*), suggesting that this neutrophil subpopulation recruited to the infected wound site might be mature but inactive (Chen et al., 2023; Evrard et al., 2018)

The infection-enriched neutrophils demonstrated a functional shift. Cluster 0 with higher expression of *Lrg1,* indicates an activated phagocytic phenotype (**Figure 5E-G**). By contrast, *Csf1*^{hi} neutrophils (cluster 2) were associated with the negative regulation of apoptosis, cytokine production and neutrophil activation. *Csf1* upregulation in neutrophils mediates macrophage differentiation towards an immunotolerant phenotype (Braza et al., 2018), characterized by low expression of the lymphocyte antigen complex (LY6C) and increased proliferation rate. We then inspected the infected myeloid cells and observed a higher abundance of the cell proliferation marker, Ki-67 (*Mki67*), and the expression of lymphocyte antigen 6 complex locus 1 (*Ly6c1*). The expression of *Mki67* was specific to terminal macrophage population clusters 2 and 5 (**Figure S5G**) and the level of *Ly6c1* was lower in all macrophages but was specific to LCs (**Figure S5H**). These findings suggest that neutrophils may contribute to the anti-inflammatory polarization of *E. faecalis* infected macrophages.

RNA velocity analysis also estimated infected neutrophils with a propensity to become *Lrg1*^{hi} neutrophils (**Figure 5H**, cluster 0), driven by genes *Entpd1*/*Cd39*, *Picalm*, *Hdc*, *Cytip*, *Sipa1l1* and *Fos* (**Figures 5I**, **S6B** and **S6C**). Moreover, suppression of *Nfkbia* and chemokine ligand-2 (*Cxcl2*) and upregulation of calprotectin (*S100a9*) together indicate an inflammatory response to *E. faecalis* infection (**Figure S6B**). To identify molecular changes that could drive neutrophil state transitions, we sorted the genes based on their peak in pseudo-time, revealing the three distinct neutrophil states: early-stage, intermediate-stage, and late-stage, in the *E. faecalis*-infected wounds (**Figure 5J**). The early response was

characterized by *Ccl6*, *Il1f9* (*Il36g*), *Cxcl2*, *S100a6,* and *S100a9*, suggesting an initial pro-inflammatory neutrophil response. By contrast, the late stage demonstrated higher expression of ribosomal proteins (*Rpl5*, *Rpl19* and *Rpl26*), migratory metalloproteinases (*Mmp3*, *Mmp19* and *Adamts5*), and CXC motif ligand-1 (*Cxcl1*), suggesting perturbed neutrophil infiltration. MMP19 has also been implicated in M2 polarization (Fingleton, 2017), consistent with the anti-inflammatory signatures of the infected macrophage populations (**Figures 4J** and **S5E**). Cellular interactome analysis further predicted the anti-inflammatory status of neutrophils by a strong correlation in the CCL signaling pathway between neutrophils and M2-like macrophages, particularly through the Ccl3:Ccr1 axis (**Figures 5K-M** and **S6D**), an interaction predictive of neutrophil extravasation during *E. faecalis* infection (Hautz et al., 2023). Neutrophil extravasation is a vital event in immune responses to infections to ensure the survival of the host (Theocharidis et al., 2022). In summary, our single-cell analysis of neutrophils during *E. faecalis* wound infection revealed a perturbed pro-inflammatory resolution during infection that may contribute to anti-inflammatory macrophage polarization. Furthermore, our findings uncover prominent differences in immune cell composition in infected wounds, featuring *Lrg1*-rich neutrophil abundance (cluster 0), together with the enrichment of *Arg1*^{hi} M2-like macrophage polarization (clusters 2 and 5). As such, wound healing during *E. faecalis* is characterized by a dysregulated immune response compared to uninfected wounds, which could be associated with delayed healing or chronic infection.

Anti-inflammatory macrophages induce pathogenic angiogenesis

Based on the role of angiogenesis in tissue repair, and our observations of the anti-inflammatory signatures provided by keratinocytes, fibroblasts, and macrophages, we investigated their impact on endothelial cells (ECs). First, we analyzed the two endothelial cell (EC) populations in the integrated dataset and identified 13 clusters with high *Pecam1* and *Plvap* expression. Notably, clusters 0 and 8 were exclusively found in the infected ECs. (**Figures 6A, 6B**, and **S7A-C**). These clusters were involved in ECM deposition, cell differentiation, and development, indicating an anti-inflammatory niche (**Figures 6C** and **6D**). Interestingly, RNA velocity analysis of infected ECs showed a faster velocity in the *Sparc*^{hi} (cluster 0) and *Cilp*^{hi} (cluster 8) cells, suggesting a dynamic transcriptional state (**Figure 6E**). The top lineage driver genes *Malat1*, *Tcf4*, *Rlcb1*, *Diaph2*, *Bmpr2,* and *Adamts9* indicate a pathogenic mechanism in proliferating ECs (**Figure 6F**).

We then explored whether the anti-inflammatory characteristics observed in infected epithelial cells, fibroblasts, and immune cells impacted ECs. To predict these cellular interactions, we conducted a differential NicheNet analysis (Browaeys et al., 2020), which involved linking the expression of ligands with corresponding receptors and downstream target gene expressions of these pairs in our scRNA-seq atlas of infected cells. Remarkably, NicheNet analysis revealed Il1b ligand of M2-like macrophages, correlated with the expression of target genes such as biglycan (*Bgn*), *Cd14*, *Ccl3*, *Csf3r*, *Itgam* and *Tnf* in ECs (**Figures 6G** and **S7D**), in line with previous studies (Perrault et al., 2018; Vu et al., 2022). Notably, BGN, a proteoglycan, has been associated with tumor EC signatures (Cong et al., 2021; Morimoto et al., 2021), further supporting the anti-inflammatory role of M2-like macrophages observed in the infected dataset. Moreover, the infection-induced expression of *Cd14* in EC suggests Toll-like receptor (TLR) activation (Dauphinee & Karsan, 2006; Lloyd & Kubes, 2006). Cell-cell interaction analysis also predicted that the Ptgs2, Spp1 and Il1a ligand activity in M2-like macrophages influenced the expression of target genes such as calprotectin (*S100a8* and *S100a9*) and colony-stimulating factor 3 (*Csf3*) These interactions suggest a potential disruption of EC integrity in the presence of *E. faecalis* infection. Similarly, according to the CellChat analysis, ECs exhibited activation of the SPP1 and CXCL signaling pathways (**Figures 6H-J**, **S7E** and **S7F**). Expression of the ligands Spp1, Cxcl2 and Cxcl3 were abundant in keratinocytes, fibroblasts, and M2-like macrophages during the infection (**Figure 6J**). In the uninfected ECs, however, fibroblasts modulated the expression of target genes such as TEK tyrosine kinase (*Tek*), Forkhead box protein O1 (*Foxo1*) and selectin-E (*Sele*), with notable angiopoietin 1 activity (**Figure S7D**), pointing to normal endothelial cell activity.

During unperturbed wound healing, macrophages modulate angiogenesis by producing proteases, including matrix metalloproteinases (MMPs), which help degrade the extracellular matrix in the wound bed. Additionally, macrophages secrete chemotactic factors such as TNF-α, VEGF and TGF-β to promote the EC migration (Du Cheyne et al., 2020; Wilkinson & Hardman, 2020). Furthermore, the TGF-β signaling pathway induces fibroblast proliferation and ECM production in wound healing (Cutroneo, 2007; Pakyari et al., 2013). Our analysis of the cellular interactome in the uninfected wound dataset revealed strong interactions in the TGF-β and VEGF signaling pathways (**Figure S7H-I**), corroborating previous studies (Joost et al., 2016; Vu et al., 2022). These findings suggest that uninfected wounds undergo reparative angiogenesis while *E. faecalis* infection evokes pathological

438 vascularization. Overall, our analysis underlines the M2-like macrophage-EC interactions as targets of

439 altered cell-cell signaling during bacteria-infected wound healing.

DISCUSSION

Wound healing is an intricate process that involves the cooperation of various cellular and extracellular components. Disruptions to this network can perturb the healing dynamics. Previous scRNA-seq studies have primarily focused on the transcriptional profiles of epithelial and fibroblast populations in wound healing (Deng et al., 2021; Haensel et al., 2020; Joost et al., 2020; Joost et al., 2018; Joost et al., 2016). However, the impact of the host-pathogen interactions on wound healing transcriptional programs remains to be investigated. Here, our work presents the first comprehensive single-cell atlas of mouse skin wounds following infection, highlighting the transcriptional aberration in wound healing. *E. faecalis* has immunosuppressive activity in various tissues and infection sites (Chong et al., 2017; Kao et al., 2023; Kao & Kline, 2019; Tien et al., 2017). By surveying approximately 23,000 cells, we identified cell types, characterized shared and distinct transcriptional programs, and delineated terminal phenotypes and signaling pathways in homeostatic healing or bacterial wound infections. These scRNA-seq findings elucidate the immunosuppressive role of *E. faecalis* during wound infections, providing valuable insights into the underlying mechanisms.

To explore the cellular landscape of *E. faecalis*-infected wounds and the impact of infection on wound healing, we focused on cell types specifically enriched in these tissues. Our analysis revealed infection-activated transcriptional states in keratinocytes, fibroblasts, and immune cells. The presence of clusters 0 and 6, exclusive to the epithelial dataset, along with RNA velocity analysis pointing to *Zeb2*-expressing cells (**Figure 2I**), suggests a potential role of *E. faecalis* in promoting a partial EMT in keratinocytes. We also identified a terminal keratinocyte population (cluster 2) at 4 dpi, characterized by the consumption of *Krt77* and *Krtdap* over pseudo-time, confirming terminal keratinocyte differentiation (**Figures 2I and S2C**). By contrast, uninfected wounds showed proliferating keratinocyte (*Mki67*^{hi}) and hair follicle (*Lrg5*^{hi}) cells (**Figure 2H**), consistent with previous findings on wound healing and skin maintenance signatures (Joost et al., 2020; Joost et al., 2018). Furthermore, we found two infection-specific fibroblast populations enriched in *Lyz2*/*Tagln* and *Timp1*, identifying their myofibroblast characteristics. The RNA velocity analysis confirmed cluster 5 as the terminal fibroblast population derived from myofibroblasts (cluster 2) (**Figure 3I**). Additionally, an increase in *Timp1* expression correlated with cell growth and proliferation signatures (*Sparc*, *Fgf7* and *Malat1*) over latent time in

cluster 5 (**Figures S4C and S4D**). These findings collectively demonstrate a profibrotic state in fibroblasts driven by *E. faecalis*-induced transcriptional dynamics.

To investigate the impact of immunosuppressive signatures in keratinocytes and fibroblasts, we examined how *E. faecalis* infection influenced the immune response in wounds. Given that prolonged macrophage survival is associated with impaired wound healing (Kim & Nair, 2019; Krzyszczyk et al., 2018), we primarily focused on the macrophage populations. We identified subpopulations of M2-like macrophages expressing *Arg1*, *Ptgs2* and *Sparc* genes (**Figure 4F-I**). COX-2 (cyclooxygenase-2, encoded by *Ptgs2* gene) has been reported as a crucial regulator of M2-like polarization in tumor-associated macrophages (Na et al., 2013; Wang et al., 2021). While macrophage polarization is complex in humans and other higher organisms (Orecchioni et al., 2019; Watanabe et al., 2019), our scRNA-seq data suggests that *E. faecalis* infection drives an anti-inflammatory microenvironment resembling the tumor microenvironment. These findings confirm and expand on previous studies highlighting the immunosuppressive role of *E. faecalis* in different contexts (Chong et al., 2017; Kao & Kline, 2019; Tien et al., 2017).

Our findings also elaborate on the potential cell-cell communication and signaling pathways involved in wound healing. Ligand-receptor interaction analysis revealed an immune-suppressive ecosystem driven by M2-like macrophages during bacterial infection (**Figure 6G**). CellChat analysis confirmed that M2-like macrophages play a crucial role in regulating angiogenesis through the Vegfa:Vegfr1 ligand-receptor pair (**Figures 6H**, **6I**, **S7E**, **S7F**, and **Table S6**). Further, the Spp1 ligand correlated with integrins (Itgav+Itgb1, Itgav+Itgb3, Itga5+Itgb1) and the cluster of differentiation receptor Cd44 in ECs. Notably, while the Spp1 ligand of macrophages registered strong interactions with ECs, infected keratinocytes and fibroblasts were identified as the primary sources of Spp1 ligand. The infection-specific abundance of *Spp1* in these clusters highlight a partial EMT state in our extended analyses (**Figures 2E-I**). Furthermore, the interaction between Spp1 and Cd44 in M2-like macrophages and ECs indicated a proliferative state. The neutrophil chemokine *Cxcl2*, which promotes wound healing and angiogenesis (Girbl et al., 2018; Sawant et al., 2021), strongly correlated with the atypical chemokine receptor *Ackr1*, suggesting neutrophil extravasation. Additionally, the secretion of heparin-binding epidermal growth factor (*Hbegf*) by keratinocytes and epiregulin-enriched fibroblasts (*Ereg*^{hi}) further

confirmed the presence of an anti-inflammatory microenvironment and angiogenic ECs in bacteria-infected wounds (**Figures 6H**, **6I**, and **S7F**).

In summary, our study provides insights into the cellular landscape, transcriptional programs, and signaling pathways associated with uninfected and *E. faecalis*-infected skin wounds. We confirm the immune-suppressive role of *E. faecalis* in wound healing, consistent with previous findings in different experimental settings (Chong et al., 2017; Kao et al., 2023; Tien et al., 2017Kao, 2023 #134). Importantly, we identify specific ligand-receptor pairs and signaling pathways affected during wound infection. The increased number of predicted signaling interactions suggests that *E. faecalis* modulates cellular communication to alter the immune response. Notably, the CXCL/SPP1 signaling pathway emerges as a critical player in shaping the immune-altering ecosystem during wound healing, highlighting its potential as a therapeutic target for chronic infections. Collectively, our findings demonstrate the collaborative role of keratinocytes, fibroblasts, and immune cells in immune suppression through CXCL/SPP1 signaling, providing new avenues for the treatment of chronic wound infections.

LIMITATIONS OF THE STUDY

Our study provides a comprehensive comparison of the transcriptomic and cellular communication profiles between uninfected and *E. faecalis*-infected full-thickness mouse skin wounds at four days post-infection. However, our study lacks a reference dataset of uninfected, unwounded dorsal skin transcriptome, which would have allowed us to investigate transcriptomic changes temporally, especially induced by the wounding alone. Although we explored public datasets to address this limitation (Haensel et al., 2020; Vu et al., 2022), the low number of cells in public datasets, particularly for macrophage populations (data not shown), prevented their inclusion in our analysis. Additionally, the absence of multiple time points hinders our ability to examine temporal changes and the dynamic kinetics of host responses following infection.

METHODS

KEY RESOURCES TABLE

REAGENT or RESOURCE	SOURCE	IDENTIFIER
Chemicals		
Bovine serum albumin	Merck	A7030
Brain Heart Infusion medium	Merck	53286
Collagenase type I	Thermo Fisher Scientific	17100017
Dispase II	Thermo Fisher Scientific	17105041
Dulbecco's phosphate buffered saline w/o Ca2+ and Mg2+	Thermo Fisher Scientific	141900094
Hank's balanced salt solution w/o Ca^{2+} and Mg^{2+}	Thermo Fisher Scientific	88284
Isoflurane	Vetpharma Animal Health	NA
Liberase TM	Merck	5401119001
Luna SYBR Green	New England Biolabs	M3003
Nair Moisturising Hair Removal Cream	Chruch and Dwight Co	NA
Recombinant Mouse M-CSF	BioLegend	576404
Phosphate buffered saline	Gibco	14190144
TRIzol	Invitrogen	15596018
Trypsin/EDTA	Gibco	25-051-CI
Chromium Next GEM Chip G Single Cell Kit	10x Genomics	1000127
Chromium Next GEM Single Cell 3' Gel Bead Kit v3.1	10x Genomics	1000129
Chromium Next GEM Single Cell 3' GEM Kit v3.1	10x Genomics	1000130
Chromium Next GEM Single Cell 3' Kit v3.1	10x Genomics	1000269
Critical Commercial Assays		
Dual Index Kit TT Set A	10x Genomics	1000215
EZ-10 DNAaway RNA Mini-Preps kit	Bio Basic	BS88136-250
Library Construction Kit	10x Genomics	1000196
RevertAid Reverse Transcriptase	Thermo Fisher	01327685
Tube, Dynabeads MyOne SILANE	10x Genomics	2000048
Bacterial Strains		
Enterococcus faecalis OG1RF	Dunny *et al*. (Dunny et al., 1978)	WT OG1RF
Oligonucleotides		
Gene	Forward	Reverse
ActB	ATC AGC AAG CAG GAG TAC GAT	GTG TAA AAC GCA GCT CAG TAA CA

Arg1	CAG AAG AAT GGA AGA GTC AG	CAG ATA TGC AGG GAG TCA CC
Egf	TGG CTC GAA GTC AGA TCC ACA	TTC TCG GGC ACA TGG TTA ATG
Gapdh	TCA GGA GAG TGT TTC CTC GTC CC	TCT CGG CCT TGA CTG TGC CG
Fgf1	CCC TGA CCG AGA GGT TCA AC	GTC CCT TGT CCC ATC CAC G
Mrc1	TTC AGC TAT TGG ACG CGA GG	GAA TCT GAC ACC CAG CGG AA
Nos2	TGT CGC AGC TCC CTA TCT TG	GGA AGC CAC TGA CAC TTC GC
Pdgfa	TGG CTC GAA GTC AGA TCC ACA	TTC TCG GGC ACA TGG TTA ATG
Tgfb1	GGA AAT CAA CGG GAT CAG CCC	GCT GCC GCA CAC AGC AGT TC
Ubc	CCC AGT GTT ACC ACC AAG AAG	CCC CAT CAC ACC CAA GAA CA
Deposited Data		
Raw and processed scRNA-seq data	NCBI Gene Expression Omnibus	GSE229257
Processed Seurat Object	Zenodo	https://doi.org/10.5281/zenodo.7608212
Experiment Models: Organisms/Strain		
Mouse C57BL/6	InVivos	n/a
Software and Algorithms		
anndata 0.8.0	PyPI	https://pypi.org
BioRender	https://biorender.com	n/a
CellChat 1.6.1	Jin *et al*. (Jin et al., 2021)	Jin *et al*. (Jin et al., 2021)
cellrank 1.5.1	Lange *et al*. (Lange et al., 2022)	Lange *et al*. (Lange et al., 2022)
Cell Ranger 6.1.2	10X Genomics, Inc.	https://www.10xgenomics.com
clustree 0.5.0	Zappia *et al*. (Zappia & Oshlack, 2018)	Zappia *et al*. (Zappia & Oshlack, 2018)
glmGamPoi 1.8.0	Ahlmann-Eltze *et al*. (Ahlmann-Eltze & Huber, 2021)	Ahlmann-Eltze *et al*. (Ahlmann-Eltze & Huber, 2021)
miQC 1.4.0	GitHub	https://github.com/greenelab/miQC
NicheNet	Browaeys *et al*. (Browaeys et al., 2020)	Browaeys *et al*. (Browaeys et al., 2020)
numpy 1.23.5	PyPI	https://pypi.org
pandas 1.5.3	PyPI	https://pypi.org
PanglaoDB	PanglaoDB	https://panglaodb.se/markers.html
Prism 9.4.1	GraphPad Software	https://www.graphpad.com
PyCharm 2022.3.3	JetBrains	https://www.jetbrains.com
Python 3.9.16	Python Software Foundation	https://python.org
R 4.2.1	The R Foundation	https://www.r-project.org
RStudio 2022.07.2+576	Posit Software	https://posit.co
samtools 1.13	GitHub	https://github.com/samtools
scanpy 1.9.1	PyPI	https://pypi.org
scipy 1.10.0	PyPI	https://pypi.org
scDblFinder 1.10.0	Germain *et al*. (Germain et al., 2021)	Germain *et al*. (Germain et al., 2021)

sctransform 0.3.5	Choudhary *et al.* (Choudhary & Satija, 2022)	Choudhary *et al.* (Choudhary & Satija, 2022)
scvelo 0.2.5	Bergen *et al.* (Bergen et al., 2020)	Bergen *et al.* (Bergen et al., 2020)
Seurat 4.3.0	Hao *et al.* (Hao et al., 2021)	Hao *et al.* (Hao et al., 2021)
UMAP	McInnes *et al.* (McInnes et al., 2018)	https://github.com/lmcinnes/umap
velocyto.py 0.17.17	La Manno *et al.* (La Manno et al., 2018)	La Manno *et al.* (La Manno et al., 2018)
WGCNA 1.72-1	Langfelder *et al.* (Langfelder & Horvath, 2008)	Langfelder *et al.* (Langfelder & Horvath, 2008)

RESOURCE AVAILABILITY

Lead Contact

Further information and requests for resources should be directed to and will be fulfilled by the lead contacts, Kimberly Kline, at kimberly.kline@unige.ch and Guillaume Thibault, at thibault@ntu.edu.sg.

Material Availability

This study did not generate new reagents.

Data and Code Availability

The accession number for the raw data reported in this paper is GSE229257. The processed data are available at Zenodo (https://doi.org/10.5281/zenodo.7608212).

METHOD DETAILS

Mouse wound infection model

In vivo procedures were approved by the Animal Care and Use Committee of the Biological Resource Centre (Nanyang Technological University, Singapore) in accordance with the guidelines of the Agri-Food and Veterinary Authority and the National Advisory Committee for Laboratory Animal Research of Singapore (ARF SBS/NIEA-0314). Male C57BL/6 mice were housed at the Research Support Building animal facility under pathogen-free conditions. Mice between 5-7 weeks old (22–25 g; InVivos, Singapore) were used for the wound infection model, modified from a previous study (Keogh et al., 2016). Briefly, mice were anesthetized with 3% isoflurane. Dorsal hair was removed by shaving, followed by hair removal cream (Nair cream, Church and Dwight Co) application. The shaven skin was then disinfected with 70% ethanol and a 6-mm full-thickness wound was created using a biopsy punch

(Integra Miltex, New York). Two mice were infected with 10 µl of 2 x10^8 bacteria/ml inoculum (*Enterococcus faecalis* OG1RF strain), while the other two served as controls for uninfected wounds. All wounds were sealed with transparent dressing (Tegaderm, 3M, St Paul Minnesota). Mice were euthanized four days post-infection (4 dpi), and wounds collected immediately using a biopsy punch with minimal adjacent healthy skin were stored in Hanks 'Buffered Salt Solution (HBSS; Ca^{2+}/Mg^{2+}-free; Sigma Aldrich, Cat. #H4385) supplemented with 0.5% bovine serum albumin (BSA; Sigma Aldrich, Cat. #A7030).

In vitro culture and infection of bone marrow-derived macrophages

Murine bone marrow-derived macrophages (BMDMs) were isolated from bone marrow cells of 7-8 weeks old C57BL/6 male mice as described previously (Toda et al., 2021), except that BMDMs were differentiated in 100 mm non-treated square dishes (Thermo Scientific, Singapore) with supplementation of 50 ng/ml M-CSF (BioLegend, Singapore). On day 6, differentiated BMDMs were harvested by gentle cell scraping in Dulbecco's PBS (DPBS; Gibco, Singapore), and 10^6 BMDMs were seeded in 6-well plates using bone marrow growth medium without antibiotics. Following overnight incubation, the growth medium was replaced with complete DMEM (DMEM supplemented with 10% FBS) for *E. faecalis* infection. Log-phase *E. faecalis* OG1RF cultures were washed and normalized to an OD_{600}/ml of 0.5 in complete DMEM, equivalent to approximately 3 x 10^8 CFU/ml. BMDMs were then infected with OG1RF at a multiplicity of infection (MOI) of 10 for 1 h, followed by centrifugation at 1,000 x *g* for 5 min prior to incubation to promote BMDM-bacteria contact. For uninfected controls, complete DMEM was added instead of MOI 10 bacterial suspension. At 1 hpi, BMDM were washed thrice with DPBS and incubated in complete DMEM supplemented with 10 µg/ml vancomycin and 150 µg/ml gentamicin for 23 h to kill extracellular bacteria, until a final time point of 24 hpi.

Quantitative qPCR analysis

Total mRNA was extracted using the TRIzol reagent (Invitrogen, cat. # 15596018) and purified using an EZ-10 DNAaway RNA Mini-Preps Kit (Bio Basic, cat. #BS88136-250). Complementary DNA (cDNA) was synthesized from total RNA using RevertAid Reverse Transcriptase (Thermo Fisher, Waltham, MA, cat. # 01327685) according to the manufacturer's protocol. Real-time PCR was performed using Luna SYBR Green (New England Biolabs, UK) according to the manufacturer's protocol using a CFX-96

Real-time PCR system (Bio-Rad, Hercules, CA, USA). A 100-ng of cDNA and 0.25 µM of the paired primer mix for target genes were used for each reaction. Relative mRNA was normalized to the housekeeping gene glyceraldehyde-3-phosphate dehydrogenase (*Gapdh*) or a geometric mean of Ct values from beta-actin (*Actb*) and ubiquitin (*Ubc*) housekeeping genes, as calculated by BestKeeper (Pfaffl et al., 2004) and log2 fold changes were plotted with reference to the uninfected, unwounded skin. The primer pairs used in this study are listed in the Key Resources Table.

Dissociation of tissue and library preparation

Tissues were transferred to a sterile 10 mm^2 tissue culture dish and cut into small fragments using a sterile blade. The dissociation cocktail [10 mg/ml of dispase II (GIBCO, Cat. #17105041), 250 mg/ml of collagenase type I (GIBCO, cat. #17100017), and 2.5 mg/ml of liberase TM (Roche, cat. #5401119001)] was dissolved in HBSS. The tissue was digested enzymatically in pre-warmed dissociation buffer for 2 h at 37°C with manual orbital shaking every 15 min and then the dissociated cells were sifted through a sterile 70-µm cell strainer (Corning, cat. #352350) on ice and washed thrice with HBSS supplemented with 0.04% BSA. The remaining undigested tissue on the filter was re-incubated in 0.05%$^{w/v}$ trypsin/EDTA (GIBCO, cat. #25-051-CI) for 15 min at 37°C. Trypsin-digested cells were pooled with cells on ice by sifting through a sterile 70-µm cell strainer. The pooled cell suspension was washed thrice with HBSS supplemented with 0.04% BSA, followed by final filtering using a sterile 40-µm cell strainer (Corning, cat. #352340). The cell suspensions were centrifuged at 300 x *g* for 10 min, and the pellets were resuspended in Dulbecco's phosphate-buffered saline (DPBS; Thermo Fisher Scientific, cat. #14190094). Cell viability was determined by using Countess 3 FL Automated Cell Counter (Invitrogen) by mixing cell suspension with 0.4% trypan blue stain (Invitrogen, cat. #T10282) at a ratio of 1:1 for a minimum of four counts per sample. Isolated cells were encapsulated for single-cell RNA sequencing with microfluidic partitioning using the Chromium Single Cell 3' Reagent Kits (v3.1 Chemistry Dual Index, Protocol #CG000315), targeting 8,000 cells (10X Genomics, Pleasanton, CA). Libraries then were pooled by condition and sequenced on the HiSeq6000 system by NovogeneAIT (Singapore). A detailed protocol can be found at protocols.io (dx.doi.org/10.17504/protocols.io.yxmvmn8m9g3p/v1).

Data Processing

Raw data (.bcl) was used as an input to *Cell Ranger* (v6.1.2, 10X Genomics) with `mkfastq` function for trimming, base calling, and demultiplexing of reads by NovogeneAIT (Singapore). FASTQ files were aligned, filtered, barcoded and UMI counted using `cellranger count` command using *GENCODE vM23/Ensembl 98* (https://cf.10xgenomics.com/supp/cell-exp/refdata-gex-GRCh38-2020-A.tar.gz) mouse reference genome with `--expect cells` of 8,000 per sample on the National Supercomputer Centre Singapore (NSCC) High Power Computing platform (ASPIRE 1). The raw data can be found at Gene Expression Omnibus with the accession number GSE229257.

Integration and downstream analysis

Datasets from each sample were integrated using *Seurat* version 4.3.0 (Hao et al., 2021) on *R* (v4.2.1) using *RStudio* interface (RStudio 2022.07.2+576 "Spotted Wakerobin" release) on macOS Ventura (13.0.1). Briefly, Seurat objects were created based on the criteria of a minimum of 3 cells expressing a minimum of 200 features. Low-quality cells were determined by a probabilistic approach using the *miQC* package (v1.4.0). Similarly, doublets were removed with *scDblFinder* v1.10.0 (Germain et al., 2021). Cell cycle stages were determined by using *Seurat*'s built-in updated cell-cycle gene list. Feature counts were normalized using `SCTransform()` v2 regularization (Choudhary & Satija, 2022) with a scaling factor of $1x10^4$ and Gamma-Poisson Generalized Linear Model by `glmGamPoi()` function (Ahlmann-Eltze & Huber, 2021), during which cell cycles and mitochondrial genes were regressed out for integration of 3,000 anchors. Fourteen principal components (PC) were included in dimension reduction calculated by the point where the change of percentage of variation was more than 0.1% between the two consecutive PCs. First, *k*-Nearest Neighbors were computed using *pca* reduction, followed by identifying original Louvain clusters with a resolution of 0.7 calculated by *clustree* v0.5.0 (Zappia & Oshlack, 2018). Uniform Manifold Approximation and Projection (UMAP) was used for visualization throughout the study (McInnes et al., 2018). A log 2-fold-change of 0.5 was set to identify gene expression markers for all clusters with `min.pct` of 0.25. Density plots were generated in the *Nebulosa* (v1.6.0) package to demonstrate specific cell population signatures. Finally, we computed weighted gene co-expression networks for describing the correlation patterns among genes across samples (Langfelder & Horvath, 2008). We also compared the 2D UMAP representations of the two conditions. Using the integrated dataset, we split the dataset based on the conditions by the built-in

`SplitObject()` function of the Seurat package. Then, we computed a cross-entropy test for the UMAP projections by applying a two-sided Kolmogorov-Smirnov test (Roca et al., 2023).

Cell type annotation

An unbiased cell annotation was conducted at two levels using the *ScType* algorithm with slight modifications (Ianevski et al., 2022). First, we identified mega classes using gene set signatures on PanglaoDB (https://panglaodb.se/; Acc. date August 2022). Secondly, we further detailed each cluster based on published comprehensive mouse skin datasets (Joost et al., 2020; Joost et al., 2016). The processed Seurat object can be found at Zenodo (https://doi.org/10.5281/zenodo.7608212).

Cell-cell interactions

NicheNet's differential *R* implementation (v1.1.1) was used to interrogate cell-cell interactions (Browaeys et al., 2020). Three databases provided, namely *ligand-target prior model*, *ligand-receptor network*, and *weighted integrated networks*, were used *NicheNet*'s *Seurat* wrapper where endothelial cells were set as the receiver (receptor) cell population, and keratinocytes, fibroblasts, and macrophages were defined as the sender (ligand) populations. The *NicheNet* heat map was plotted to visualize the ligand activity-target cell gene expression matrix. We further compared cell-cell interactions between different niches to better predict niche-specific ligand-receptor (L-R) pairs using differential *NicheNet* analysis. *CellChat* (v1.6.1) was used to further identify secreted ligand-receptor pairs across all cell populations (Jin et al., 2021).

RNA velocity analysis

BAM files generated during the alignment of the raw data in Cell Ranger, were sorted by cell barcodes with `sort -t CB` using *samtools* (v1.13) in the command line. Spliced and unspliced reads were annotated in *velocyto.py* (v0.17.17) pipeline (La Manno et al., 2018), with repeats mask annotation file downloaded from https://genome.ucsc.edu/ for mouse reference genome to generate `.loom` files. To solve full transcriptomics dynamics, we used the generalized dynamic model on *scVelo* v0.2.0 (Bergen et al., 2020) in *Python* 3 (v3.9.16) virtual environment set up in PyCharm (Education License v2022.3.3, build PY-223.8836.43; JetBrains, Czechia), and visualized main cell populations and subset analysis with velocity stream plots and individual genes that drive RNA velocity. Lineage driving genes were

computed in *CellRank* v1.5.1 (Lange et al., 2022). Annotated data (`anndata`) files for each cell population and condition can be found at https://doi.org/10.5281/zenodo.7608772. The R scripts and complete *Jupyter* notebooks are also available at https://github.com/cenk-celik/Celik_et_al.

Statistical analysis

Statistical analyses were performed in *R*, python and Prism 9 (v9.4.1, GraphPad) whichever was applicable for the type of analysis. *P* values were adjusted with the Benjamini-Hochberg method for high-dimensional data analysis. The details of the significance and type of the test were indicated in the figure legends. Data are expressed as median ± SEM. A p-value of 0.05 was set as a significance threshold unless stated otherwise.

ACKNOWLEDGEMENTS

We are grateful to Drs. Claudia Stocks and Sophie Janssens for helpful discussions and critical reading of the manuscript. We thank the Singapore Centre for Environmental Life Sciences Engineering High Throughput Sequencing Unit for providing us with the Chromium Controller (10X Genomics) microfluidic partitioning instrument for single-cell encapsulation. The computational work for this article was partially performed on resources of the National Supercomputing Centre (NSCC), Singapore. This work was supported by funds from the National Medical Research Council Open Fund (MOH-000566 to K.A.K. and G.T. and MOH-000645 to K.A.K.), the Singapore Ministry of Education Academic Research Fund Tier 2 (MOE2019-T2-2-089 to K.A.K.), NTU Research Scholarship to S.Y.T.L. (predoctoral fellowship), and Nanyang President's Graduate Scholarship to F.R.T. Parts of this work were also supported by the National Research Foundation and Ministry of Education Singapore under its Research Centre of Excellence Program (SCELSE).

AUTHOR CONTRIBUTIONS

Conceptualization, C.C., K.A.K. and G.T.; Methodology, C.C., F.R.T., K.A.K. and G.T.; Software, C.C.; Validation, C.C.; Formal Analysis, C.C. and F.R.T.; Investigation, C.C., S.Y.T.L., F.R.T., and M.V.; Resources, C.C. and M.V., Data Curation, C.C.; Writing – Original Draft; C.C., K.A.K., and G.T.; Writing – Review & Editing, S.Y.T.L., F.R.T, K.A.K., and G.T.; Visualization, C.C. and G.T.; Supervision, K.A.K. and G.T.; Project Administration, K.A.K. and G.T.; Funding Acquisition, K.A.K. and G.T.

DECLARATION OF INTERESTS

The authors declare no competing financial interests.

ADDITIONAL FILES

Table S1. Number of cells in each Louvain cluster grouped by condition. Related to Figure 1.

Table S2. Differential expression table of genes for the main class clusters. Related to Figure 1C.

Table S3. Differential expression table of genes for the main uninfected class clusters. Related to Figure 1C.

Table S4. Differential expression table of genes for the main infected class clusters. Related to Figure 1C.

Table S5. Differential expression table of genes for sub-clustered keratinocytes. Related to Figure 2.

Table S6. CellChat comparison for ligand:receptor pairs for the uninfected and infected datasets. Related to Figures 2-6.

Table S7. Differential expression table of genes for sub-clustered fibroblasts. Related to Figure 3.

Table S8. Differential expression table of genes for sub-clustered myeloid clusters. Related to Figure 4.

Table S9. Differential expression table of genes for sub-clustered neutrophil clusters. Related to Figure 5.

REFERENCES

Ahlmann-Eltze, C., & Huber, W. (2021). glmGamPoi: fitting Gamma-Poisson generalized linear models on single cell count data. *Bioinformatics*, *36*(24), 5701-5702. https://doi.org/10.1093/bioinformatics/btaa1009

Alshetaiwi, H., Pervolarakis, N., McIntyre, L. L., Ma, D., Nguyen, Q., Rath, J. A., Nee, K., Hernandez, G., Evans, K., Torosian, L., Silva, A., Walsh, C., & Kessenbrock, K. (2020). Defining the emergence of myeloid-derived suppressor cells in breast cancer using single-cell transcriptomics. *Sci Immunol*, *5*(44). https://doi.org/10.1126/sciimmunol.aay6017

Ashcroft, K. J., Syed, F., & Bayat, A. (2013). Site-specific keloid fibroblasts alter the behaviour of normal skin and normal scar fibroblasts through paracrine signalling. *PLoS One*, *8*(12), e75600. https://doi.org/10.1371/journal.pone.0075600

Bao, Y., Sakinc, T., Laverde, D., Wobser, D., Benachour, A., Theilacker, C., Hartke, A., & Huebner, J. (2012). Role of mprF1 and mprF2 in the pathogenicity of Enterococcus faecalis. *PLoS One*, *7*(6), e38458. https://doi.org/10.1371/journal.pone.0038458

Bergen, V., Lange, M., Peidli, S., Wolf, F. A., & Theis, F. J. (2020). Generalizing RNA velocity to transient cell states through dynamical modeling. *Nat Biotechnol*, *38*(12), 1408-1414. https://doi.org/10.1038/s41587-020-0591-3

Bertuccini, L., Ammendolia, M. G., Superti, F., & Baldassarri, L. (2002). Invasion of HeLa cells by Enterococcus faecalis clinical isolates. *Med Microbiol Immunol*, *191*(1), 25-31. https://doi.org/10.1007/s00430-002-0115-4

Braza, M. S., Conde, P., Garcia, M., Cortegano, I., Brahmachary, M., Pothula, V., Fay, F., Boros, P., Werner, S. A., Ginhoux, F., Mulder, W. J. M., & Ochando, J. (2018). Neutrophil derived CSF1 induces macrophage polarization and promotes transplantation tolerance. *Am J Transplant*, *18*(5), 1247-1255. https://doi.org/10.1111/ajt.14645

Browaeys, R., Saelens, W., & Saeys, Y. (2020). NicheNet: modeling intercellular communication by linking ligands to target genes. *Nat Methods*, *17*(2), 159-162. https://doi.org/10.1038/s41592-019-0667-5

Ch'ng, J. H., Chong, K. K. L., Lam, L. N., Wong, J. J., & Kline, K. A. (2019). Biofilm-associated infection by enterococci. *Nat Rev Microbiol*, *17*(2), 82-94. https://doi.org/10.1038/s41579-018-0107-z

Chen, J., Bai, Y., Xue, K., Li, Z., Zhu, Z., Li, Q., Yu, C., Li, B., Shen, S., Qiao, P., Li, C., Luo, Y., Qiao, H., Dang, E., Yin, W., Gudjonsson, J. E., Wang, G., & Shao, S. (2023). CREB1-driven CXCR4(hi) neutrophils promote skin inflammation in mouse models and human patients. *Nat Commun*, *14*(1), 5894. https://doi.org/10.1038/s41467-023-41484-3

Cheng, J. B., Sedgewick, A. J., Finnegan, A. I., Harirchian, P., Lee, J., Kwon, S., Fassett, M. S., Golovato, J., Gray, M., Ghadially, R., Liao, W., Perez White, B. E., Mauro, T. M., Mully, T., Kim, E. A., Sbitany, H., Neuhaus, I. M., Grekin, R. C., Yu, S. S., Gray, J. W., Purdom, E., Paus, R., Vaske, C. J., Benz, S. C., Song, J. S., & Cho, R. J. (2018). Transcriptional Programming of Normal and Inflamed Human Epidermis at Single-Cell Resolution. *Cell Rep*, *25*(4), 871-883. https://doi.org/10.1016/j.celrep.2018.09.006

Cheng, M., Liang, G., Yin, Z., Lin, X., Sun, Q., & Liu, Y. (2023). Immunosuppressive role of SPP1-CD44 in the tumor microenvironment of intrahepatic cholangiocarcinoma assessed by single-cell RNA sequencing. *J Cancer Res Clin Oncol*, *149*(9), 5497-5512. https://doi.org/10.1007/s00432-022-04498-w

Cheng, T. Y., Wu, M. S., Lin, J. T., Lin, M. T., Shun, C. T., Hua, K. T., & Kuo, M. L. (2014). Formyl Peptide receptor 1 expression is associated with tumor progression and survival in gastric cancer. *Anticancer Res*, *34*(5), 2223-2229. https://www.ncbi.nlm.nih.gov/pubmed/24778024

Chong, K. K. L., Tay, W. H., Janela, B., Yong, A. M. H., Liew, T. H., Madden, L., Keogh, D., Barkham, T. M. S., Ginhoux, F., Becker, D. L., & Kline, K. A. (2017). Enterococcus faecalis Modulates Immune Activation and Slows Healing During Wound Infection. *J Infect Dis*, *216*(12), 1644-1654. https://doi.org/10.1093/infdis/jix541

Choudhary, S., & Satija, R. (2022). Comparison and evaluation of statistical error models for scRNA-seq. *Genome Biol*, *23*(1), 27. https://doi.org/10.1186/s13059-021-02584-9

Cong, L., Maishi, N., Annan, D. A., Young, M. F., Morimoto, H., Morimoto, M., Nam, J. M., Hida, Y., & Hida, K. (2021). Inhibition of stromal biglycan promotes normalization of the tumor microenvironment and enhances chemotherapeutic efficacy. *Breast Cancer Res*, *23*(1), 51. https://doi.org/10.1186/s13058-021-01423-w

Cuervo, H., Guerrero, N. A., Carbajosa, S., Beschin, A., De Baetselier, P., Girones, N., & Fresno, M. (2011). Myeloid-derived suppressor cells infiltrate the heart in acute Trypanosoma cruzi infection. *J Immunol*, *187*(5), 2656-2665. https://doi.org/10.4049/jimmunol.1002928

778 Cutroneo, K. R. (2007). TGF-beta-induced fibrosis and SMAD signaling: oligo decoys as natural
779 therapeutics for inhibition of tissue fibrosis and scarring. *Wound Repair Regen*, *15 Suppl 1*,
780 S54-60. https://doi.org/10.1111/j.1524-475X.2007.00226.x
781 da Silva, R. A. G., Tay, W. H., Ho, F. K., Tanoto, F. R., Chong, K. K. L., Choo, P. Y., Ludwig, A., &
782 Kline, K. A. (2022). Enterococcus faecalis alters endo-lysosomal trafficking to replicate and
783 persist within mammalian cells. *PLoS Pathog*, *18*(4), e1010434.
784 https://doi.org/10.1371/journal.ppat.1010434
785 Dauphinee, S. M., & Karsan, A. (2006). Lipopolysaccharide signaling in endothelial cells. *Lab Invest*,
786 *86*(1), 9-22. https://doi.org/10.1038/labinvest.3700366
787 Deng, C. C., Hu, Y. F., Zhu, D. H., Cheng, Q., Gu, J. J., Feng, Q. L., Zhang, L. X., Xu, Y. P., Wang, D.,
788 Rong, Z., & Yang, B. (2021). Single-cell RNA-seq reveals fibroblast heterogeneity and
789 increased mesenchymal fibroblasts in human fibrotic skin diseases. *Nat Commun*, *12*(1), 3709.
790 https://doi.org/10.1038/s41467-021-24110-y
791 Denhardt, D. T., Noda, M., O'Regan, A. W., Pavlin, D., & Berman, J. S. (2001). Osteopontin as a means
792 to cope with environmental insults: regulation of inflammation, tissue remodeling, and cell
793 survival. *J Clin Invest*, *107*(9), 1055-1061. https://doi.org/10.1172/JCI12980
794 Der, E., Suryawanshi, H., Morozov, P., Kustagi, M., Goilav, B., Ranabothu, S., Izmirly, P., Clancy, R.,
795 Belmont, H. M., Koenigsberg, M., Mokrzycki, M., Rominieki, H., Graham, J. A., Rocca, J. P.,
796 Bornkamp, N., Jordan, N., Schulte, E., Wu, M., Pullman, J., Slowikowski, K., Raychaudhuri, S.,
797 Guthridge, J., James, J., Buyon, J., Tuschl, T., Putterman, C., Accelerating Medicines
798 Partnership Rheumatoid, A., & Systemic Lupus Erythematosus, C. (2019). Tubular cell and
799 keratinocyte single-cell transcriptomics applied to lupus nephritis reveal type I IFN and fibrosis
800 relevant pathways. *Nat Immunol*, *20*(7), 915-927. https://doi.org/10.1038/s41590-019-0386-1
801 Du Cheyne, C., Tay, H., & De Spiegelaere, W. (2020). The complex TIE between macrophages and
802 angiogenesis. *Anat Histol Embryol*, *49*(5), 585-596. https://doi.org/10.1111/ahe.12518
803 Dunny, G. M., Brown, B. L., & Clewell, D. B. (1978). Induced cell aggregation and mating in
804 Streptococcus faecalis: evidence for a bacterial sex pheromone. *Proc Natl Acad Sci U S A*,
805 *75*(7), 3479-3483. https://doi.org/10.1073/pnas.75.7.3479
806 Eming, S. A., Martin, P., & Tomic-Canic, M. (2014). Wound repair and regeneration: mechanisms,
807 signaling, and translation. *Sci Transl Med*, *6*(265), 265sr266.
808 https://doi.org/10.1126/scitranslmed.3009337
809 Evrard, M., Kwok, I. W. H., Chong, S. Z., Teng, K. W. W., Becht, E., Chen, J., Sieow, J. L., Penny, H.
810 L., Ching, G. C., Devi, S., Adrover, J. M., Li, J. L. Y., Liong, K. H., Tan, L., Poon, Z., Foo, S.,
811 Chua, J. W., Su, I. H., Balabanian, K., Bachelerie, F., Biswas, S. K., Larbi, A., Hwang, W. Y.
812 K., Madan, V., Koeffler, H. P., Wong, S. C., Newell, E. W., Hidalgo, A., Ginhoux, F., & Ng, L.
813 G. (2018). Developmental Analysis of Bone Marrow Neutrophils Reveals Populations
814 Specialized in Expansion, Trafficking, and Effector Functions. *Immunity*, *48*(2), 364-379 e368.
815 https://doi.org/10.1016/j.immuni.2018.02.002
816 Fang, T., Zhang, L., Yin, X., Wang, Y., Zhang, X., Bian, X., Jiang, X., Yang, S., & Xue, Y. (2023). The
817 prognostic marker elastin correlates with epithelial-mesenchymal transition and vimentin-
818 positive fibroblasts in gastric cancer. *J Pathol Clin Res*, *9*(1), 56-72.
819 https://doi.org/10.1002/cjp2.298
820 Farr, L., Ghosh, S., & Moonah, S. (2020). Role of MIF Cytokine/CD74 Receptor Pathway in Protecting
821 Against Injury and Promoting Repair. *Front Immunol*, *11*, 1273.
822 https://doi.org/10.3389/fimmu.2020.01273
823 Fingleton, B. (2017). Matrix metalloproteinases as regulators of inflammatory processes. *Biochim*
824 *Biophys Acta Mol Cell Res*, *1864*(11 Pt A), 2036-2042.
825 https://doi.org/10.1016/j.bbamcr.2017.05.010
826 Fitzgerald, A. A., & Weiner, L. M. (2020). The role of fibroblast activation protein in health and
827 malignancy. *Cancer Metastasis Rev*, *39*(3), 783-803. https://doi.org/10.1007/s10555-020-
828 09909-3
829 Franzen, O., Gan, L. M., & Bjorkegren, J. L. M. (2019). PanglaoDB: a web server for exploration of
830 mouse and human single-cell RNA sequencing data. *Database (Oxford)*, *2019*.
831 https://doi.org/10.1093/database/baz046
832 Gao, W., Liu, D., Sun, H., Shao, Z., Shi, P., Li, T., Yin, S., & Zhu, T. (2022). SPP1 is a prognostic related
833 biomarker and correlated with tumor-infiltrating immune cells in ovarian cancer. *BMC Cancer*,
834 *22*(1), 1367. https://doi.org/10.1186/s12885-022-10485-8
835 Gentry-Weeks, C. R., Karkhoff-Schweizer, R., Pikis, A., Estay, M., & Keith, J. M. (1999). Survival of
836 Enterococcus faecalis in mouse peritoneal macrophages. *Infect Immun*, *67*(5), 2160-2165.
837 https://doi.org/10.1128/IAI.67.5.2160-2165.1999

838 Germain, P. L., Lun, A., Garcia Meixide, C., Macnair, W., & Robinson, M. D. (2021). Doublet
839 identification in single-cell sequencing data using scDblFinder. *F1000Res*, *10*, 979.
840 https://doi.org/10.12688/f1000research.73600.2
841 Girbl, T., Lenn, T., Perez, L., Rolas, L., Barkaway, A., Thiriot, A., Del Fresno, C., Lynam, E., Hub, E.,
842 Thelen, M., Graham, G., Alon, R., Sancho, D., von Andrian, U. H., Voisin, M. B., Rot, A., &
843 Nourshargh, S. (2018). Distinct Compartmentalization of the Chemokines CXCL1 and CXCL2
844 and the Atypical Receptor ACKR1 Determine Discrete Stages of Neutrophil Diapedesis.
845 *Immunity*, *49*(6), 1062-1076 e1066. https://doi.org/10.1016/j.immuni.2018.09.018
846 Gornicki, T., Lambrinow, J., Mrozowska, M., Podhorska-Okolow, M., Dziegiel, P., & Grzegrzolka, J.
847 (2022). Role of RBMS3 Novel Potential Regulator of the EMT Phenomenon in Physiological
848 and Pathological Processes. *Int J Mol Sci*, *23*(18). https://doi.org/10.3390/ijms231810875
849 Guasch, G., Schober, M., Pasolli, H. A., Conn, E. B., Polak, L., & Fuchs, E. (2007). Loss of TGFbeta
850 signaling destabilizes homeostasis and promotes squamous cell carcinomas in stratified
851 epithelia. *Cancer Cell*, *12*(4), 313-327. https://doi.org/10.1016/j.ccr.2007.08.020
852 Guerrero-Juarez, C. F., Dedhia, P. H., Jin, S., Ruiz-Vega, R., Ma, D., Liu, Y., Yamaga, K., Shestova,
853 O., Gay, D. L., Yang, Z., Kessenbrock, K., Nie, Q., Pear, W. S., Cotsarelis, G., & Plikus, M. V.
854 (2019). Single-cell analysis reveals fibroblast heterogeneity and myeloid-derived adipocyte
855 progenitors in murine skin wounds. *Nat Commun*, *10*(1), 650. https://doi.org/10.1038/s41467-
856 018-08247-x
857 Haensel, D., Jin, S., Sun, P., Cinco, R., Dragan, M., Nguyen, Q., Cang, Z., Gong, Y., Vu, R., MacLean,
858 A. L., Kessenbrock, K., Gratton, E., Nie, Q., & Dai, X. (2020). Defining Epidermal Basal Cell
859 States during Skin Homeostasis and Wound Healing Using Single-Cell Transcriptomics. *Cell*
860 *Rep*, *30*(11), 3932-3947 e3936. https://doi.org/10.1016/j.celrep.2020.02.091
861 Hao, Y., Hao, S., Andersen-Nissen, E., Mauck, W. M., 3rd, Zheng, S., Butler, A., Lee, M. J., Wilk, A. J.,
862 Darby, C., Zager, M., Hoffman, P., Stoeckius, M., Papalexi, E., Mimitou, E. P., Jain, J.,
863 Srivastava, A., Stuart, T., Fleming, L. M., Yeung, B., Rogers, A. J., McElrath, J. M., Blish, C. A.,
864 Gottardo, R., Smibert, P., & Satija, R. (2021). Integrated analysis of multimodal single-cell data.
865 *Cell*, *184*(13), 3573-3587 e3529. https://doi.org/10.1016/j.cell.2021.04.048
866 Hautz, T., Salcher, S., Fodor, M., Sturm, G., Ebner, S., Mair, A., Trebo, M., Untergasser, G., Sopper,
867 S., Cardini, B., Martowicz, A., Hofmann, J., Daum, S., Kalb, M., Resch, T., Krendl, F.,
868 Weissenbacher, A., Otarashvili, G., Obrist, P., Zelger, B., Ofner, D., Trajanoski, Z., Troppmair,
869 J., Oberhuber, R., Pircher, A., Wolf, D., & Schneeberger, S. (2023). Immune cell dynamics
870 deconvoluted by single-cell RNA sequencing in normothermic machine perfusion of the liver.
871 *Nat Commun*, *14*(1), 2285. https://doi.org/10.1038/s41467-023-37674-8
872 Hofer, F., Di Sario, G., Musiu, C., Sartoris, S., De Sanctis, F., & Ugel, S. (2021). A Complex Metabolic
873 Network Confers Immunosuppressive Functions to Myeloid-Derived Suppressor Cells
874 (MDSCs) within the Tumour Microenvironment. *Cells*, *10*(10).
875 https://doi.org/10.3390/cells10102700
876 Horsley, H., Dharmasena, D., Malone-Lee, J., & Rohn, J. L. (2018). A urine-dependent human urothelial
877 organoid offers a potential alternative to rodent models of infection. *Sci Rep*, *8*(1), 1238.
878 https://doi.org/10.1038/s41598-018-19690-7
879 Horsley, H., Malone-Lee, J., Holland, D., Tuz, M., Hibbert, A., Kelsey, M., Kupelian, A., & Rohn, J. L.
880 (2013). Enterococcus faecalis subverts and invades the host urothelium in patients with chronic
881 urinary tract infection. *PLoS One*, *8*(12), e83637. https://doi.org/10.1371/journal.pone.0083637
882 Hu, J., Ma, Y., Ma, J., Chen, S., Zhang, X., Guo, S., Huang, Z., Yue, T., Yang, Y., Ning, Y., Zhu, J.,
883 Wang, P., Wang, X., Chen, G., & Liu, Y. (2020). Macrophage-derived SPARC Attenuates M2-
884 mediated Pro-tumour Phenotypes. *J Cancer*, *11*(10), 2981-2992.
885 https://doi.org/10.7150/jca.39651
886 Ianevski, A., Giri, A. K., & Aittokallio, T. (2022). Fully-automated and ultra-fast cell-type identification
887 using specific marker combinations from single-cell transcriptomic data. *Nat Commun*, *13*(1),
888 1246. https://doi.org/10.1038/s41467-022-28803-w
889 Jager, B., Klatt, D., Plappert, L., Golpon, H., Lienenklaus, S., Barbosa, P. D., Schambach, A., & Prasse,
890 A. (2020). CXCR4/MIF axis amplifies tumor growth and epithelial-mesenchymal interaction in
891 non-small cell lung cancer. *Cell Signal*, *73*, 109672.
892 https://doi.org/10.1016/j.cellsig.2020.109672
893 Jin, S., Guerrero-Juarez, C. F., Zhang, L., Chang, I., Ramos, R., Kuan, C. H., Myung, P., Plikus, M. V.,
894 & Nie, Q. (2021). Inference and analysis of cell-cell communication using CellChat. *Nat*
895 *Commun*, *12*(1), 1088. https://doi.org/10.1038/s41467-021-21246-9

Joost, S., Annusver, K., Jacob, T., Sun, X., Dalessandri, T., Sivan, U., Sequeira, I., Sandberg, R., & Kasper, M. (2020). The Molecular Anatomy of Mouse Skin during Hair Growth and Rest. *Cell Stem Cell*, *26*(3), 441-457 e447. https://doi.org/10.1016/j.stem.2020.01.012

Joost, S., Jacob, T., Sun, X., Annusver, K., La Manno, G., Sur, I., & Kasper, M. (2018). Single-Cell Transcriptomics of Traced Epidermal and Hair Follicle Stem Cells Reveals Rapid Adaptations during Wound Healing. *Cell Rep*, *25*(3), 585-597 e587. https://doi.org/10.1016/j.celrep.2018.09.059

Joost, S., Zeisel, A., Jacob, T., Sun, X., La Manno, G., Lonnerberg, P., Linnarsson, S., & Kasper, M. (2016). Single-Cell Transcriptomics Reveals that Differentiation and Spatial Signatures Shape Epidermal and Hair Follicle Heterogeneity. *Cell Syst*, *3*(3), 221-237 e229. https://doi.org/10.1016/j.cels.2016.08.010

Kandaswamy, K., Liew, T. H., Wang, C. Y., Huston-Warren, E., Meyer-Hoffert, U., Hultenby, K., Schroder, J. M., Caparon, M. G., Normark, S., Henriques-Normark, B., Hultgren, S. J., & Kline, K. A. (2013). Focal targeting by human beta-defensin 2 disrupts localized virulence factor assembly sites in Enterococcus faecalis. *Proc Natl Acad Sci U S A*, *110*(50), 20230-20235. https://doi.org/10.1073/pnas.1319066110

Kao, P. H., Ch'ng, J. H., Chong, K. K. L., Stocks, C. J., Wong, S. L., & Kline, K. A. (2023). Enterococcus faecalis suppresses Staphylococcus aureus-induced NETosis and promotes bacterial survival in polymicrobial infections. *FEMS Microbes*, *4*, xtad019. https://doi.org/10.1093/femsmc/xtad019

Kao, P. H. N., & Kline, K. A. (2019). Dr. Jekyll and Mr. Hide: How Enterococcus faecalis Subverts the Host Immune Response to Cause Infection. *J Mol Biol*, *431*(16), 2932-2945. https://doi.org/10.1016/j.jmb.2019.05.030

Keogh, D., Tay, W. H., Ho, Y. Y., Dale, J. L., Chen, S., Umashankar, S., Williams, R. B. H., Chen, S. L., Dunny, G. M., & Kline, K. A. (2016). Enterococcal Metabolite Cues Facilitate Interspecies Niche Modulation and Polymicrobial Infection. *Cell Host Microbe*, *20*(4), 493-503. https://doi.org/10.1016/j.chom.2016.09.004

Kim, S. Y., & Nair, M. G. (2019). Macrophages in wound healing: activation and plasticity. *Immunol Cell Biol*, *97*(3), 258-267. https://doi.org/10.1111/imcb.12236

Krzyszczyk, P., Schloss, R., Palmer, A., & Berthiaume, F. (2018). The Role of Macrophages in Acute and Chronic Wound Healing and Interventions to Promote Pro-wound Healing Phenotypes. *Front Physiol*, *9*, 419. https://doi.org/10.3389/fphys.2018.00419

La Manno, G., Soldatov, R., Zeisel, A., Braun, E., Hochgerner, H., Petukhov, V., Lidschreiber, K., Kastriti, M. E., Lonnerberg, P., Furlan, A., Fan, J., Borm, L. E., Liu, Z., van Bruggen, D., Guo, J., He, X., Barker, R., Sundstrom, E., Castelo-Branco, G., Cramer, P., Adameyko, I., Linnarsson, S., & Kharchenko, P. V. (2018). RNA velocity of single cells. *Nature*, *560*(7719), 494-498. https://doi.org/10.1038/s41586-018-0414-6

Landen, N. X., Li, D., & Stahle, M. (2016). Transition from inflammation to proliferation: a critical step during wound healing. *Cell Mol Life Sci*, *73*(20), 3861-3885. https://doi.org/10.1007/s00018-016-2268-0

Lange, M., Bergen, V., Klein, M., Setty, M., Reuter, B., Bakhti, M., Lickert, H., Ansari, M., Schniering, J., Schiller, H. B., Pe'er, D., & Theis, F. J. (2022). CellRank for directed single-cell fate mapping. *Nat Methods*, *19*(2), 159-170. https://doi.org/10.1038/s41592-021-01346-6

Langfelder, P., & Horvath, S. (2008). WGCNA: an R package for weighted correlation network analysis. *BMC Bioinformatics*, *9*, 559. https://doi.org/10.1186/1471-2105-9-559

Li, X., Zhai, Y., Xi, B., Ma, W., Zhang, J., Ma, X., Miao, Y., Zhao, Y., Ning, W., Zhou, H., & Yang, C. (2021). Pinocembrin Ameliorates Skin Fibrosis via Inhibiting TGF-beta1 Signaling Pathway. *Biomolecules*, *11*(8). https://doi.org/10.3390/biom11081240

Lindley, L. E., Stojadinovic, O., Pastar, I., & Tomic-Canic, M. (2016). Biology and Biomarkers for Wound Healing. *Plast Reconstr Surg*, *138*(3 Suppl), 18S-28S. https://doi.org/10.1097/PRS.0000000000002682

Lloyd, K. L., & Kubes, P. (2006). GPI-linked endothelial CD14 contributes to the detection of LPS. *Am J Physiol Heart Circ Physiol*, *291*(1), H473-481. https://doi.org/10.1152/ajpheart.01234.2005

Maloney, J., Keselman, A., Li, E., & Singer, S. M. (2015). Macrophages expressing arginase 1 and nitric oxide synthase 2 accumulate in the small intestine during Giardia lamblia infection. *Microbes Infect*, *17*(6), 462-467. https://doi.org/10.1016/j.micinf.2015.03.006

Masson-Meyers, D. S., Andrade, T. A. M., Caetano, G. F., Guimaraes, F. R., Leite, M. N., Leite, S. N., & Frade, M. A. C. (2020). Experimental models and methods for cutaneous wound healing assessment. *Int J Exp Pathol*, *101*(1-2), 21-37. https://doi.org/10.1111/iep.12346

Mattila, J. T., Ojo, O. O., Kepka-Lenhart, D., Marino, S., Kim, J. H., Eum, S. Y., Via, L. E., Barry, C. E., 3rd, Klein, E., Kirschner, D. E., Morris, S. M., Jr., Lin, P. L., & Flynn, J. L. (2013). Microenvironments in tuberculous granulomas are delineated by distinct populations of macrophage subsets and expression of nitric oxide synthase and arginase isoforms. *J Immunol*, *191*(2), 773-784. https://doi.org/10.4049/jimmunol.1300113

McInnes, L., Healy, J., & Melville, J. (2018). Umap: Uniform manifold approximation and projection for dimension reduction. *arXiv preprint arXiv:1802.03426*.

Meister, M., Tounsi, A., Gaffal, E., Bald, T., Papatriantafyllou, M., Ludwig, J., Pougialis, G., Bestvater, F., Klotz, L., Moldenhauer, G., Tuting, T., Hammerling, G. J., Arnold, B., & Oelert, T. (2015). Self-Antigen Presentation by Keratinocytes in the Inflamed Adult Skin Modulates T-Cell Auto-Reactivity. *J Invest Dermatol*, *135*(8), 1996-2004. https://doi.org/10.1038/jid.2015.130

Minutti, C. M., Knipper, J. A., Allen, J. E., & Zaiss, D. M. (2017). Tissue-specific contribution of macrophages to wound healing. *Semin Cell Dev Biol*, *61*, 3-11. https://doi.org/10.1016/j.semcdb.2016.08.006

Mizumoto, S., Janecke, A. R., Sadeghpour, A., Povysil, G., McDonald, M. T., Unger, S., Greber-Platzer, S., Deak, K. L., Katsanis, N., Superti-Furga, A., Sugahara, K., Davis, E. E., Yamada, S., & Vodopiutz, J. (2020). CSGALNACT1-congenital disorder of glycosylation: A mild skeletal dysplasia with advanced bone age. *Hum Mutat*, *41*(3), 655-667. https://doi.org/10.1002/humu.23952

Morimoto, H., Hida, Y., Maishi, N., Nishihara, H., Hatanaka, Y., Li, C., Matsuno, Y., Nakamura, T., Hirano, S., & Hida, K. (2021). Biglycan, tumor endothelial cell secreting proteoglycan, as possible biomarker for lung cancer. *Thorac Cancer*, *12*(9), 1347-1357. https://doi.org/10.1111/1759-7714.13907

Munadziroh, E., Askandar, M. G., Yuliati, A., Surboyo, M. D. C., & Wan Harun, W. H. A. (2022). The effect of secretory leukocyte protease inhibitor amnion membrane on incisional wound healing. *J Oral Biol Craniofac Res*, *12*(3), 358-362. https://doi.org/10.1016/j.jobcr.2022.04.001

Na, Y. R., Yoon, Y. N., Son, D. I., & Seok, S. H. (2013). Cyclooxygenase-2 inhibition blocks M2 macrophage differentiation and suppresses metastasis in murine breast cancer model. *PLoS One*, *8*(5), e63451. https://doi.org/10.1371/journal.pone.0063451

Nunez, N., Derre-Bobillot, A., Trainel, N., Lakisic, G., Lecomte, A., Mercier-Nome, F., Cassard, A. M., Bierne, H., Serror, P., & Archambaud, C. (2022). The unforeseen intracellular lifestyle of Enterococcus faecalis in hepatocytes. *Gut Microbes*, *14*(1), 2058851. https://doi.org/10.1080/19490976.2022.2058851

Olmsted, S. B., Dunny, G. M., Erlandsen, S. L., & Wells, C. L. (1994). A plasmid-encoded surface protein on Enterococcus faecalis augments its internalization by cultured intestinal epithelial cells. *J Infect Dis*, *170*(6), 1549-1556. https://doi.org/10.1093/infdis/170.6.1549

Orecchioni, M., Ghosheh, Y., Pramod, A. B., & Ley, K. (2019). Macrophage Polarization: Different Gene Signatures in M1(LPS+) vs. Classically and M2(LPS-) vs. Alternatively Activated Macrophages. *Front Immunol*, *10*, 1084. https://doi.org/10.3389/fimmu.2019.01084

Pakyari, M., Farrokhi, A., Maharlooei, M. K., & Ghahary, A. (2013). Critical Role of Transforming Growth Factor Beta in Different Phases of Wound Healing. *Adv Wound Care (New Rochelle)*, *2*(5), 215-224. https://doi.org/10.1089/wound.2012.0406

Perrault, D. P., Bramos, A., Xu, X., Shi, S., & Wong, A. K. (2018). Local Administration of Interleukin-1 Receptor Antagonist Improves Diabetic Wound Healing. *Ann Plast Surg*, *80*(5S Suppl 5), S317-S321. https://doi.org/10.1097/SAP.0000000000001417

Pfaffl, M. W., Tichopad, A., Prgomet, C., & Neuvians, T. P. (2004). Determination of stable housekeeping genes, differentially regulated target genes and sample integrity: BestKeeper--Excel-based tool using pair-wise correlations. *Biotechnol Lett*, *26*(6), 509-515. https://doi.org/10.1023/b:bile.0000019559.84305.47

Philippeos, C., Telerman, S. B., Oules, B., Pisco, A. O., Shaw, T. J., Elgueta, R., Lombardi, G., Driskell, R. R., Soldin, M., Lynch, M. D., & Watt, F. M. (2018). Spatial and Single-Cell Transcriptional Profiling Identifies Functionally Distinct Human Dermal Fibroblast Subpopulations. *J Invest Dermatol*, *138*(4), 811-825. https://doi.org/10.1016/j.jid.2018.01.016

Rashid, R., Nair, Z. J., Chia, D. M. H., Chong, K. K. L., Cazenave Gassiot, A., Morley, S. A., Allen, D. K., Chen, S. L., Chng, S. S., Wenk, M. R., & Kline, K. A. (2023). Depleting Cationic Lipids Involved in Antimicrobial Resistance Drives Adaptive Lipid Remodeling in Enterococcus faecalis. *mBio*, *14*(1), e0307322. https://doi.org/10.1128/mbio.03073-22

Recalcati, S., Gammella, E., Buratti, P., Doni, A., Anselmo, A., Locati, M., & Cairo, G. (2019). Macrophage ferroportin is essential for stromal cell proliferation in wound healing. *Haematologica*, *104*(1), 47-58. https://doi.org/10.3324/haematol.2018.197517

Roca, C. P., Burton, O. T., Neumann, J., Tareen, S., Whyte, C. E., Gergelits, V., Veiga, R. V., Humblet-Baron, S., & Liston, A. (2023). A cross entropy test allows quantitative statistical comparison of t-SNE and UMAP representations. *Cell Rep Methods*, *3*(1), 100390. https://doi.org/10.1016/j.crmeth.2022.100390

Rognoni, E., & Watt, F. M. (2018). Skin Cell Heterogeneity in Development, Wound Healing, and Cancer. *Trends Cell Biol*, *28*(9), 709-722. https://doi.org/10.1016/j.tcb.2018.05.002

Sawant, K. V., Sepuru, K. M., Lowry, E., Penaranda, B., Frevert, C. W., Garofalo, R. P., & Rajarathnam, K. (2021). Neutrophil recruitment by chemokines Cxcl1/KC and Cxcl2/MIP2: Role of Cxcr2 activation and glycosaminoglycan interactions. *J Leukoc Biol*, *109*(4), 777-791. https://doi.org/10.1002/JLB.3A0820-207R

Schultz, G., Rotatori, D. S., & Clark, W. (1991). EGF and TGF-alpha in wound healing and repair. *J Cell Biochem*, *45*(4), 346-352. https://doi.org/10.1002/jcb.240450407

Siriwach, R., Ngo, A. Q., Narumiya, S., & Thumkeo, D. (2022). An optimized protocol to identify keratinocyte subpopulations in vitro by single-cell RNA sequencing analysis. *STAR Protoc*, *3*(4), 101906. https://doi.org/10.1016/j.xpro.2022.101906

Standal, T., Borset, M., & Sundan, A. (2004). Role of osteopontin in adhesion, migration, cell survival and bone remodeling. *Exp Oncol*, *26*(3), 179-184. https://www.ncbi.nlm.nih.gov/pubmed/15494684

Takaoka, R. T. C., Sertorio, N. D., Magalini, L. P. J., Dos Santos, L. M., Souza, H. R., Iyomasa-Pilon, M. M., Possebon, L., Costa, S. S., & Girol, A. P. (2018). Expression profiles of Annexin A1, formylated peptide receptors and cyclooxigenase-2 in gastroesophageal inflammations and neoplasias. *Pathol Res Pract*, *214*(2), 181-186. https://doi.org/10.1016/j.prp.2017.12.003

Tamoutounour, S., Han, S. J., Deckers, J., Constantinides, M. G., Hurabielle, C., Harrison, O. J., Bouladoux, N., Linehan, J. L., Link, V. M., Vujkovic-Cvijin, I., Perez-Chaparro, P. J., Rosshart, S. P., Rehermann, B., Lazarevic, V., & Belkaid, Y. (2019). Keratinocyte-intrinsic MHCII expression controls microbiota-induced Th1 cell responses. *Proc Natl Acad Sci U S A*, *116*(47), 23643-23652. https://doi.org/10.1073/pnas.1912432116

Tan, C. A. Z., Lam, L. N., Biukovic, G., Soh, E. Y., Toh, X. W., Lemos, J. A., & Kline, K. A. (2022). Enterococcus faecalis Antagonizes Pseudomonas aeruginosa Growth in Mixed-Species Interactions. *J Bacteriol*, *204*(7), e0061521. https://doi.org/10.1128/jb.00615-21

Theocharidis, G., Rahmani, S., Lee, S., Li, Z., Lobao, A., Kounas, K., Katopodi, X. L., Wang, P., Moon, S., Vlachos, I. S., Niewczas, M., Mooney, D., & Veves, A. (2022). Murine macrophages or their secretome delivered in alginate dressings enhance impaired wound healing in diabetic mice. *Biomaterials*, *288*, 121692. https://doi.org/10.1016/j.biomaterials.2022.121692

Tien, B. Y. Q., Goh, H. M. S., Chong, K. K. L., Bhaduri-Tagore, S., Holec, S., Dress, R., Ginhoux, F., Ingersoll, M. A., Williams, R. B. H., & Kline, K. A. (2017). Enterococcus faecalis Promotes Innate Immune Suppression and Polymicrobial Catheter-Associated Urinary Tract Infection. *Infect Immun*, *85*(12). https://doi.org/10.1128/IAI.00378-17

Toda, G., Yamauchi, T., Kadowaki, T., & Ueki, K. (2021). Preparation and culture of bone marrow-derived macrophages from mice for functional analysis. *STAR Protoc*, *2*(1), 100246. https://doi.org/10.1016/j.xpro.2020.100246

Vecchi, L., Alves Pereira Zoia, M., Goss Santos, T., de Oliveira Beserra, A., Colaco Ramos, C. M., Franca Matias Colombo, B., Paiva Maia, Y. C., Piana de Andrade, V., Teixeira Soares Mota, S., Goncalves de Araujo, T., Van Petten de Vasconcelos Azevedo, F., Soares, F. A., Oliani, S. M., & Goulart, L. R. (2018). Inhibition of the AnxA1/FPR1 autocrine axis reduces MDA-MB-231 breast cancer cell growth and aggressiveness in vitro and in vivo. *Biochim Biophys Acta Mol Cell Res*, *1865*(9), 1368-1382. https://doi.org/10.1016/j.bbamcr.2018.06.010

Veglia, F., Sanseviero, E., & Gabrilovich, D. I. (2021). Myeloid-derived suppressor cells in the era of increasing myeloid cell diversity. *Nat Rev Immunol*, *21*(8), 485-498. https://doi.org/10.1038/s41577-020-00490-y

Vu, R., Jin, S., Sun, P., Haensel, D., Nguyen, Q. H., Dragan, M., Kessenbrock, K., Nie, Q., & Dai, X. (2022). Wound healing in aged skin exhibits systems-level alterations in cellular composition and cell-cell communication. *Cell Rep*, *40*(5), 111155. https://doi.org/10.1016/j.celrep.2022.111155

Wang, M., Chaudhuri, R., Ong, W. W. S., & Sintim, H. O. (2021). c-di-GMP Induces COX-2 Expression in Macrophages in a STING-Independent Manner. *ACS Chem Biol*, *16*(9), 1663-1670. https://doi.org/10.1021/acschembio.1c00342

Wang, P. H., Huang, B. S., Horng, H. C., Yeh, C. C., & Chen, Y. J. (2018). Wound healing. *J Chin Med Assoc*, *81*(2), 94-101. https://doi.org/10.1016/j.jcma.2017.11.002

Watanabe, S., Alexander, M., Misharin, A. V., & Budinger, G. R. S. (2019). The role of macrophages in the resolution of inflammation. *J Clin Invest*, *129*(7), 2619-2628. https://doi.org/10.1172/JCI124615

Wells, C. L., Jechorek, R. P., & Erlandsen, S. L. (1990). Evidence for the translocation of Enterococcus faecalis across the mouse intestinal tract. *J Infect Dis*, *162*(1), 82-90. https://doi.org/10.1093/infdis/162.1.82

Wells, C. L., Jechorek, R. P., Maddaus, M. A., & Simmons, R. L. (1988). Effects of clindamycin and metronidazole on the intestinal colonization and translocation of enterococci in mice. *Antimicrob Agents Chemother*, *32*(12), 1769-1775. https://doi.org/10.1128/AAC.32.12.1769

Wilkinson, H. N., & Hardman, M. J. (2020). Wound healing: cellular mechanisms and pathological outcomes. *Open Biol*, *10*(9), 200223. https://doi.org/10.1098/rsob.200223

Xie, Y., Gao, K., Hakkinen, L., & Larjava, H. S. (2009). Mice lacking beta6 integrin in skin show accelerated wound repair in dexamethasone impaired wound healing model. *Wound Repair Regen*, *17*(3), 326-339. https://doi.org/10.1111/j.1524-475X.2009.00480.x

Yang, Y. H., Aeberli, D., Dacumos, A., Xue, J. R., & Morand, E. F. (2009). Annexin-1 regulates macrophage IL-6 and TNF via glucocorticoid-induced leucine zipper. *J Immunol*, *183*(2), 1435-1445. https://doi.org/10.4049/jimmunol.0804000

Zappia, L., & Oshlack, A. (2018). Clustering trees: a visualization for evaluating clusterings at multiple resolutions. *Gigascience*, *7*(7). https://doi.org/10.1093/gigascience/giy083

Zhao, L., Wang, W., Niu, P., Luan, X., Zhao, D., & Chen, Y. (2022). The molecular mechanisms of CTHRC1 in gastric cancer by integrating TCGA, GEO and GSA datasets. *Front Genet*, *13*, 900124. https://doi.org/10.3389/fgene.2022.900124

Zou, J., & Shankar, N. (2014). Enterococcus faecalis infection activates phosphatidylinositol 3-kinase signaling to block apoptotic cell death in macrophages. *Infect Immun*, *82*(12), 5132-5142. https://doi.org/10.1128/IAI.02426-14

Zou, J., & Shankar, N. (2016). The opportunistic pathogen Enterococcus faecalis resists phagosome acidification and autophagy to promote intracellular survival in macrophages. *Cell Microbiol*, *18*(6), 831-843. https://doi.org/10.1111/cmi.12556

FIGURE LEGENDS

Figure 1. Mouse skin wound infection atlas.

(A) Gene expression of healing markers *Pdgfa*, *Tgfb1* and *Egf* four days post-infection (4 dpi) for uninfected and *E. faecalis*-infected 6–7-week-old C57BL/6J mouse skin wounds, normalized to intact skin (n = 6 for skin; n = 8 for wounds; one-way ANOVA). **(B)** Single-cell RNA sequencing workflow of full-thickness mouse wounds. **(C)** Integrated dataset of ~23,000 scRNA-seq libraries from uninfected and infected wounds identifies 5 mega cell classes indicated in the UMAP. **(D)** UMAP colored by the uninfected and infected conditions. **(E)** Schematic describing the color-matched cell types with that of the clusters in Figure S1F. **(F)** Dot plot depicting the top two cell type-specific markers in the integrated data. Legend indicates average expression and dot size represents percent expression. **(G)** Density plots depict cell types described in C. **(H)** Heat map of weighted gene co-expression network analysis for annotated cell populations, colored by bars matching mega clusters and annotated cell types in C.

Figure 2. Sub-clustering of keratinocyte populations reveals infection-specific cell types.

(A) UMAP of integrated keratinocyte (basal, suprabasal, hair follicle, bulge, and sebaceous gland) population reveals 19 clusters. **(B)** Infected keratinocytes (green) show unique and shared clusters with uninfected keratinocytes (purple). **(C)** Spatial dispersion of *Krt5* and *Krt10* abundance in keratinocytes. **(D)** Expression of *Lgr5*, *Ivl*, *Lor*, and *Krt15* in Louvain clusters shown in A. **(E)** Heat map of top 5 differentially expressed marker genes for each cluster in keratinocytes. Rectangle boxes indicate infection-specific Louvain clusters. **(F-G)** The bar plots show the top 15 Gene Ontology terms for infection-specific (F) *Zeb2*^{hi} (cluster 0) and (G) *Gjb6*^{hi} (cluster 6) keratinocyte populations. **(H-I)** Dynamic RNA velocity estimation of uninfected (H) and infected (I) keratinocytes. **(J)** The top lineage driver gene, *Rgs1*, in infected keratinocytes, was ubiquitously expressed in infection-specific Louvain clusters. (K) Gene expression dynamics resolved along latent time in the top 50 likelihood-ranked genes of infected keratinocytes. The colored bar at the top indicates Louvain clusters in I. Legend describes scaled gene expression. (L) Inferred ligand-receptor pairs outgoing from infected keratinocytes. (M) The hierarchy tree depicts the trajectory of differentiating and terminally differentiated keratinocyte cells originating from basal keratinocytes.

Figure 3. *E. faecalis* delays immune response in fibroblasts.

(A) UMAP of integrated fibroblasts reveals 12 clusters. **(B)** Infected fibroblasts (green) show unique and shared clusters with uninfected fibroblasts (purple). **(C)** Spatial dispersion of *Col1a1* and *Col1a2* abundance in fibroblasts. **(D)** Expression of *Eln*, *Aspn*, *Pdgfrb* and *Fap* in Louvain clusters shown in A. **(E)** Heat map of top 5 differentially expressed marker genes for each cluster in fibroblasts. Rectangle boxes indicate infection-specific Louvain clusters. **(F-G)** The bar plots show the top 15 Gene Ontology terms for infection-specific (F) *Lyz2*^{hi}/*Tagln*^{hi} (cluster 0) and (G) *Timp1*^{hi} (cluster 2) fibroblast populations. **(H-I)** Dynamic RNA velocity estimation of uninfected (H) and infected (I) fibroblasts. **(J)** The top lineage driver gene, *Csgalnac1*, expression in infected fibroblasts. **(K)** Gene expression dynamics resolved along latent time in the top 50 likelihood-ranked genes of infected fibroblasts. The colored bar at the top indicates Louvain clusters in I. Legend describes scaled gene expression. **(L)** While uninfected fibroblasts show healing phenotypes, infected fibroblasts undergo two transitioning phases: (i) contractile and (ii) pathologic.

Figure 4. Macrophages display M2-like polarization.

(A) UMAP of the integrated myeloid population reveals 9 macrophages, 2 dendritic cells, and one Langerhans cell cluster. **(B)** Infected myeloid (green) population show unique and shared clusters with the uninfected myeloid (purple) population. **(C)** Spatial distribution of *Lyz2* (macrophage) and *Itgax* (DC and LC) abundance in fibroblasts. **(D)** Gene expression *Mrc1*, *Nos2* and *Arg1* in mouse wounds at 4dpi, normalized to homeostatic skin (n = 6 for skin; n = 8 for wounds; one-way ANOVA). **(E)** *In vitro* infection of unpolarized (M0) bone marrow-derived murine macrophages (BMDMs) resulted in a down-regulation of TRM-associated marker *Mrc1* and an upregulation of M2-like markers *Nos2* and *Arg1*. Data are pooled from 2 biological replicates (shown in light and dark circles respectively) of 3 technical replicates each. **(F)** Spatial distribution of TRM and M2-like macrophage markers, *Mrc1* and *Arg1*, respectively. **(G)** Expression of *Mrc1*, *Adgre1*, *Arg1, Itgax*, *Cd207* and *Nos2* in the integrated myeloid dataset. **(H-I)** Dynamic RNA velocity estimation of uninfected (H) and infected (I) myeloid cells. **(J)** The top lineage driver gene, *Fth1*, was ubiquitously expressed in terminal macrophage populations. **(K)** Putative driver genes of infected macrophages. **(L)** The proposed model describes macrophage characteristics, where neutrophil-attracting and wound repair-associated macrophages were involved in uninfected wound healing. In contrast, bacteria-infected wounds are enriched in efferocytotic macrophages and matrix-producing macrophages.

Figure 5. Crosstalk between neutrophils and anti-inflammatory macrophages regulates the CCL signaling pathway.

(A) UMAP of the integrated myeloid population reveals 6 Louvain clusters. **(B)** The infected neutrophil (green) population shows unique and shared clusters with the uninfected neutrophil (purple) population. **(C)** Spatial organization of *Csf3r* and *Itgam* abundance in neutrophils. **(D)** Expression of *Cxcr2*, *Fcgr3*, *Fth1* and *Camk1d* in Louvain clusters. **(E)** Heat map of top 5 differentially expressed marker genes in neutrophils. Rectangle boxes indicate infection-specific Louvain clusters. **(F-G)** The bar plots show the top 15 Gene Ontology terms for infection-specific (F) *Lrg1*^{hi} (cluster 0) and **(G)** *Csf1*^{hi} (cluster 2) populations. **(H)** Dynamic RNA velocity estimation of infected neutrophils. **(I)** The top lineage driver gene, *Entpd1*, was ubiquitously expressed in *Lrg1*^{hi} neutrophils (cluster 0). **(J)** Putative driver genes of infected neutrophil clusters. **(K)** Cytokine signaling pathway (CCL) cell-cell interaction map. **(L)** Gene expression of cytokines *Ccl3*, *Ccl4,* and *Ccl6* in neutrophils. **(M)** Ccl3:Ccr1 ligand-receptor interaction mediate neutrophil-macrophage crosstalk.

Figure 6. Macrophage-EC interactions display an anti-inflammatory niche.

(A) UMAP of integrated endothelial cells reveals 13 clusters. **(B)** Infected endothelial cells (green) show unique and shared clusters with uninfected endothelial cells (purple). **(C-D)** Gene Ontology analysis of infection-specific clusters 0 (C) and 8 (D). **(E)** Dynamic RNA velocity estimation of infected endothelial cells. **(F)** The top lineage driver genes, *Malat1*, *Tcf4, Plcb1, Diaph2, Bmpr2,* and *Adamts9* in infected endothelial cells. **(G)** NicheNet interaction heat map between keratinocytes, fibroblasts, macrophages, and endothelial cells. Note the macrophage *Il1b*-specific *Bgn* induction in infected ECs. **(H)** The dot plot depicts interactions between endothelial cells (receptors) and keratinocytes, fibroblasts, and macrophages (ligands). Rows demonstrate a ligand-receptor pair for the indicated cell-cell interactions (column). **(I)** Differential interaction strengths of a cellular interactome for TNF, SPP1 and CXCL signaling pathways between all cell types in infection. **(J)** Spp1, Cxcl2, and Cxcl3 gene expression in keratinocytes, M2-like macrophages, and fibroblasts (Wilcoxon Rank Sum test, ****$p < 0.0001$).

Supplemental information

Decoding the complexity of delayed wound healing following *Enterococcus faecalis* infection

Cenk CELIK, Stella Yue Ting LEE, Frederick Reinhart TANOTO, Mark VELEBA, Kimberly A. KLINE, Guillaume THIBAULT

SUPPLEMENTAL FIGURES

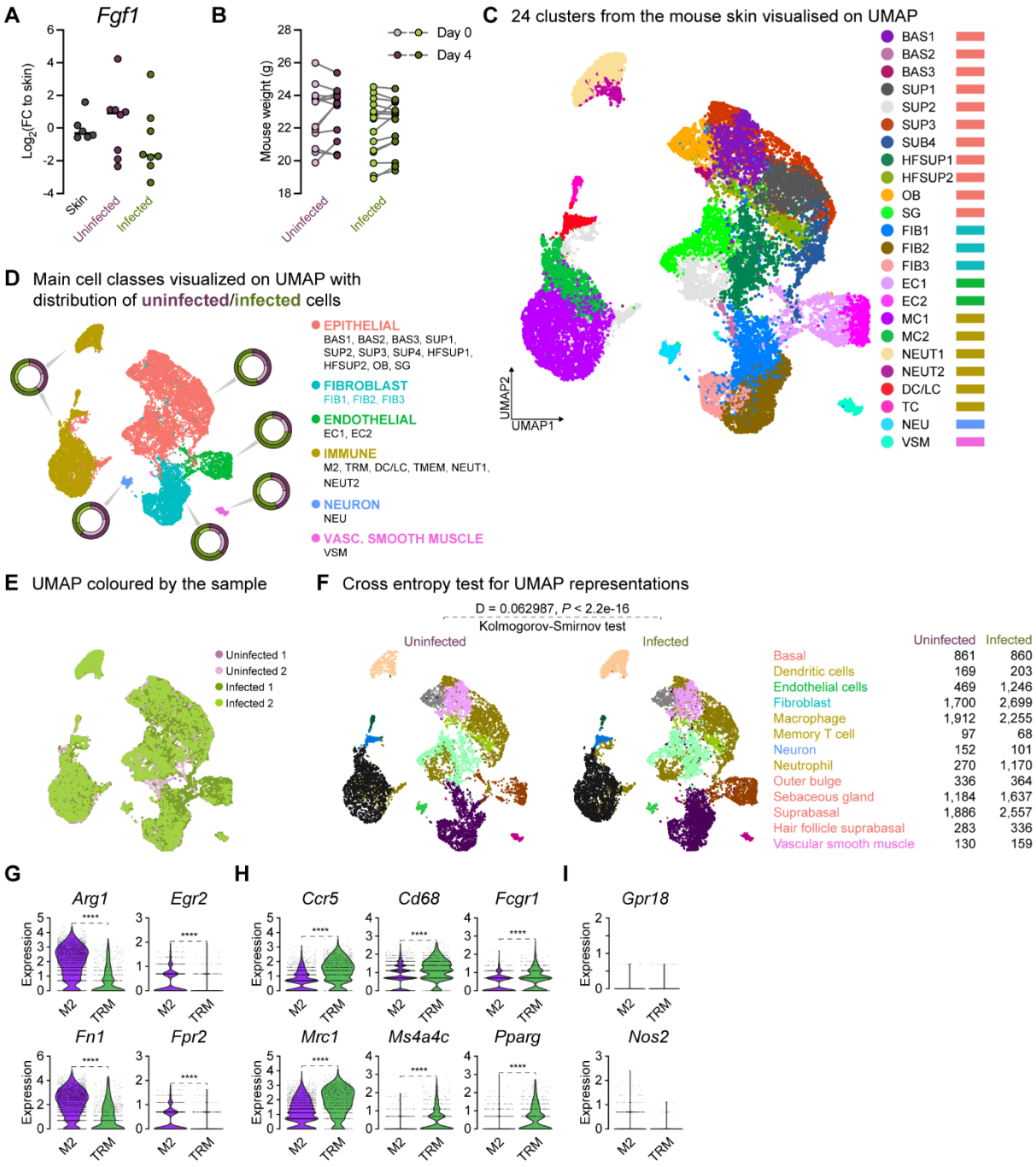

Figure S1. Comparison of 4dpi characteristics between uninfected and *E. faecalis* infected *in vivo* and scRNA-seq data.

(A) Gene expression of fibroblast growth factor 1 (*Fgf1*) four days post-infection (4dpi) for uninfected and *E. faecalis*-infected 6–7-week-old C57BL/6J mouse skin wounds, normalized to homeostatic skin (n = 6 for skin; n = 8 for wounds; one-way ANOVA). **(B)** Weight of mice from wounding (Day 0) until 4 dpi. **(C-D)** Integrated Louvain clustering of ~23,000 scRNA-seq libraries from uninfected and infected wounds identifies 24 clusters (C) in 5 mega clusters (D), where colored circles show the contribution to the individual clusters for each condition. **(E)** UMAP colored by the sample, where shades of purple and green represent uninfected and infected conditions, respectively. **(F)** Cross entropy test for UMAP representations of uninfected and infected single-cell datasets (P value < 2.2 x 10^{-16}, two-sided Kolmogorov-Smirnov test). **(G-I)** Comparisons of M2-like macrophage polarization (M2) markers *Arg1*, *Egr2*, *Fn1* and *Fpr2* (G), tissue-resident macrophage (TRM) markers *Ccr5*, *Cd68*, *Fcgr1*, *Mrc1* (*Cd206*),

Ms4a4c, and *Pparg* (H), and M1-like macrophage polarization markers *Grp18* and *Nos2* (*iNos*) between the two annotated macrophage clusters (I). Wilcoxon Rank Sum test, ****$p < 0.0001$.

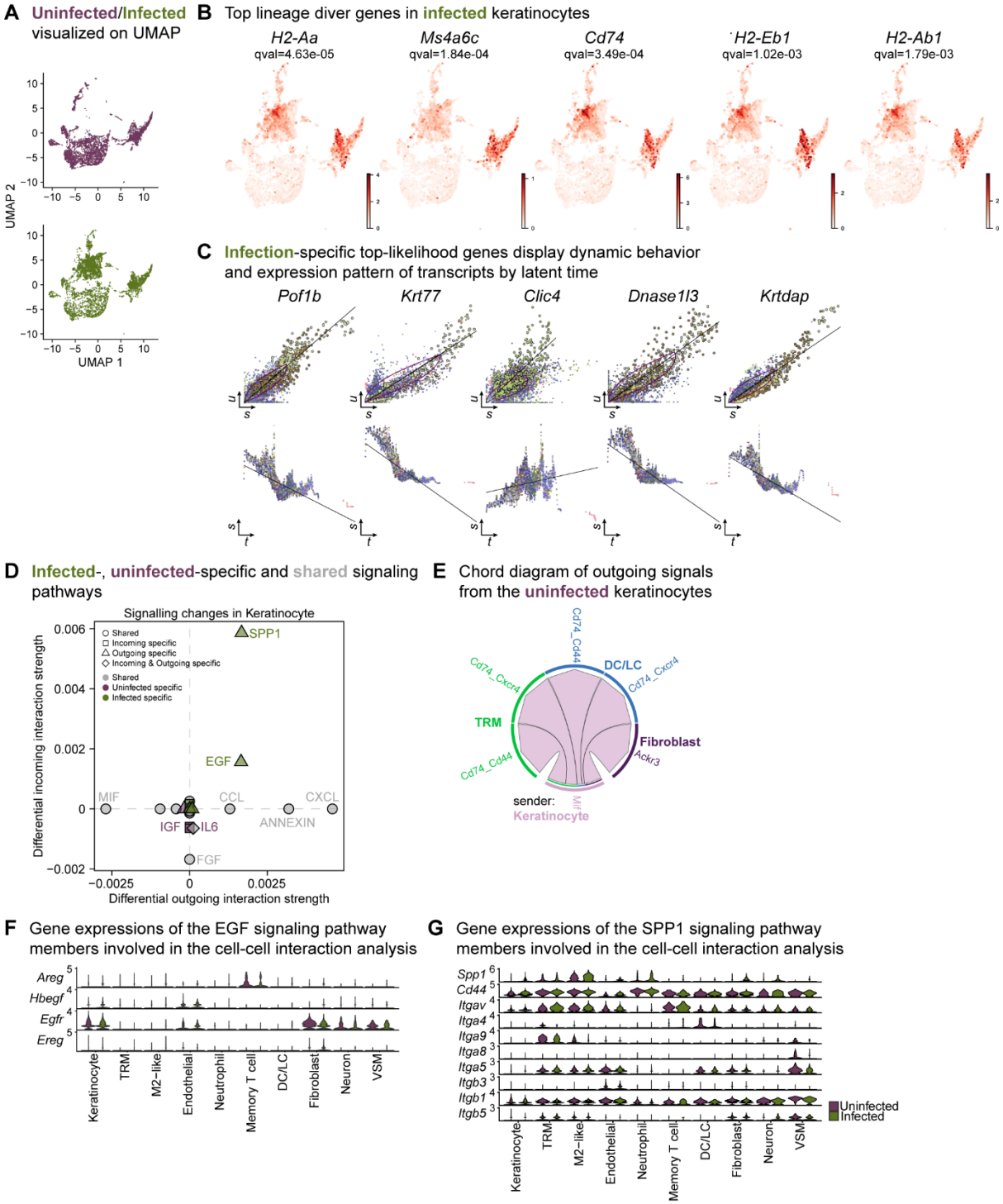

Figure S2. Infection-specific keratinocytes display differential transcriptome.
(A) UMAP representations of the extended analysis of keratinocytes from uninfected and infected wounds. **(B)** The lineage driver genes, *H2-Aa*, *Ms4a6c*, *Cd74*, *H2-Eb1* and *H2-Ab1* in infected keratinocytes were ubiquitously expressed in infection-specific Louvain clusters. **(C)** Infection-specific top-likelihood genes display dynamic behavior (top row) and expression pattern of transcripts by latent time (bottom row). Axes denote *u* for unspliced; *s* for spliced; *t* for latent time. **(D)** Infected- (green), uninfected-specific (purple) and shared (grey) signaling pathways in keratinocytes inferred from CellChat. **(E)** Chord diagram of outgoing signals from the uninfected keratinocyte population. **(F-G)** Gene expression of the EGF (F) and SPP1 (G) signaling pathway members involved in the cell-cell interaction analysis.

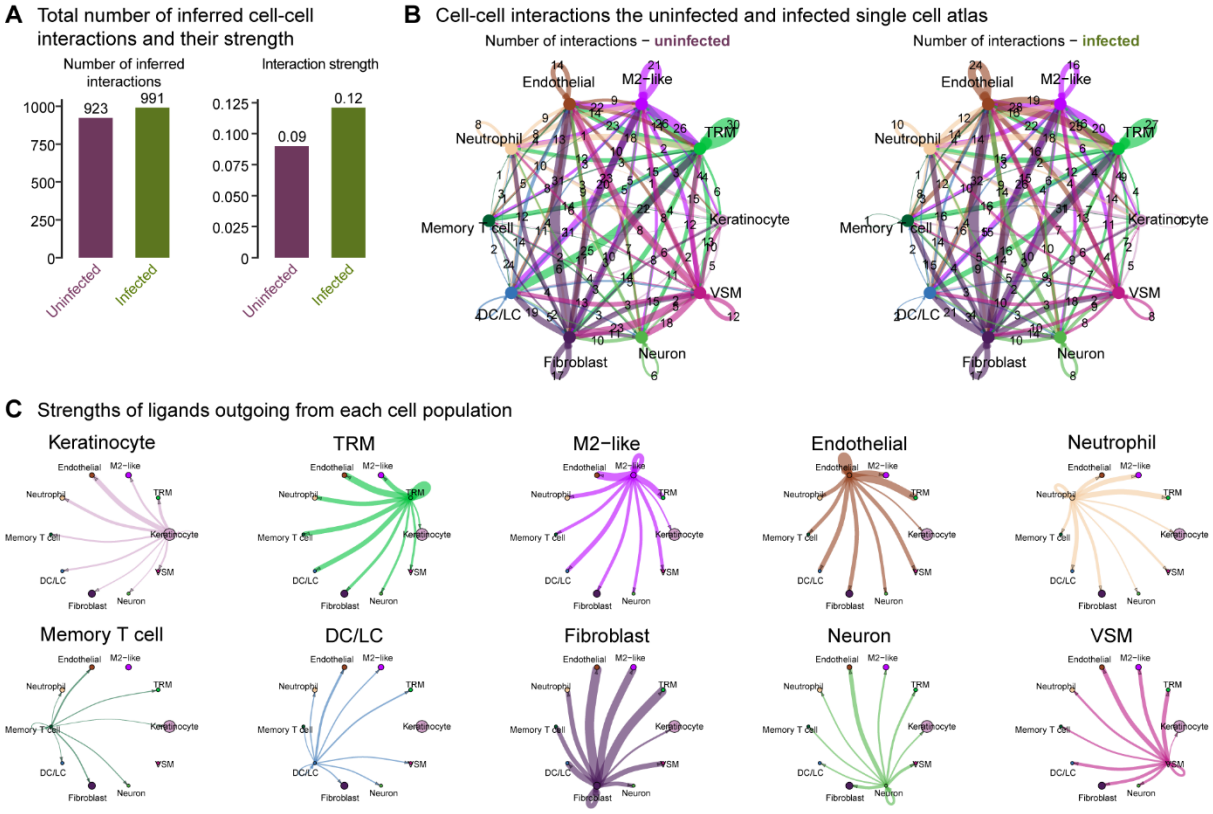

Figure S3. Overall cellular interactome of scRNA-seq atlas.
(A) Total number of inferred cell-cell interactions and their strength computed by CellChat. **(B)** A map of cell-cell interactions in the uninfected and infected single-cell atlas, indicating the number of interactions outgoing at each node. **(C)** The strengths of ligands outgoing from each cell population.

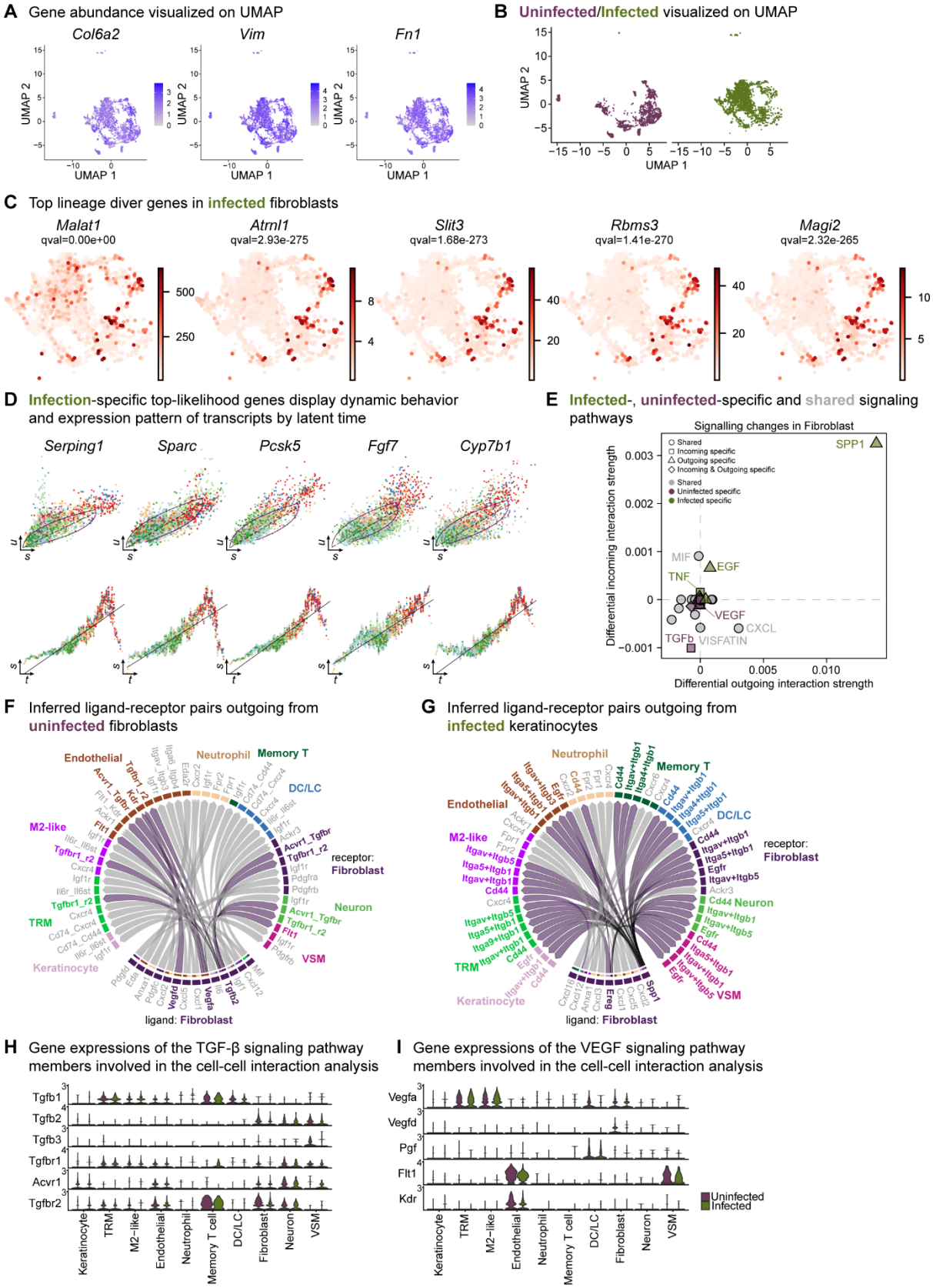

Figure S4. Extended analysis of the fibroblast population reveals unique signatures.
(A) Spatial dispersion of fibroblast markers *Col6a2*, *Vim,* and *Fn1* in the extended analysis integrated data. **(B)** Extended analysis of fibroblasts displays infection- and healing-specific clusters. **(C)** The lineage driver genes *Malat1*, *Atrnl1*, *Slit3*, *Rbms3,* and *Magi2* were predominantly expressed in infected fibroblasts. **(D)** Infection-specific top-likelihood genes display dynamic behavior (top row) and

expression pattern of transcripts by latent time (bottom row). Axes denote *u* for unspliced; *s* for spliced; *t* for latent time. **(E)** Infected- (green), uninfected-specific (purple) and shared (grey) signaling pathways in fibroblasts inferred from CellChat. **(F-G)** Chord diagram of ligand-receptor pairs in the uninfected (F) and infected (G) fibroblasts. **(I)** Inferred ligand-receptor pairs outgoing from infected fibroblasts **(H-I)** Gene expression of the TGF-β (F) and VEGF (G) signaling pathway members involved in the cell-cell interaction analysis.

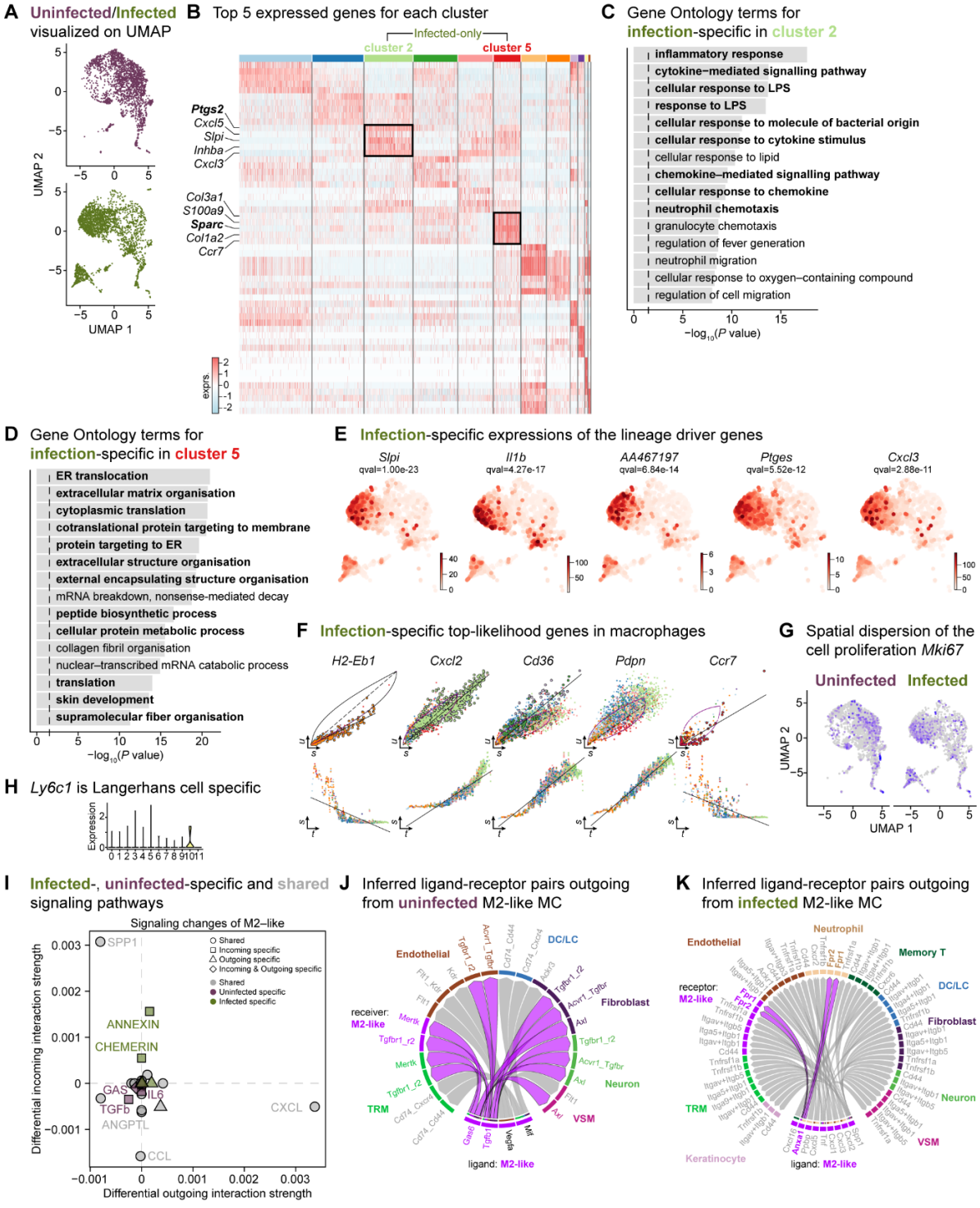

Figure S5. The mega myeloid cell population displays M2-like polarization signatures.
(A) Split UMAP representations of the uninfected and infected myeloid cells. **(B)** Heat map of top 5 differentially expressed marker genes in macrophages. Rectangle boxes indicate infection-specific Louvain clusters. **(C-D)** The bar plots show the top 15 Gene Ontology terms for infection-specific *Ptgs2*$^{+}$ (cluster 2) (C) and *Sparc*$^{+}$ (cluster 5) macrophages (D). **(E)** Infection-specific expression of the lineage driver genes *Slpi*, *Il1b*, *AA467197*, *Ptges,* and *Cxcl3* indicate delayed inflammation. **(F)** Infection-specific top-likelihood genes, *Cxcl2*, *Cd36,* and *Pdpn*, were activated, while *H2-Eb1* and *Ccr7* were consumed in macrophages. **(G)** Spatial dispersion of the cell proliferation marker (*Mki67*). **(H)** Expression of *Ly6c1* was Langerhans cell-specific. **(I)** Infected- (green), uninfected-specific (purple), and shared (grey) signaling pathways in M2-like macrophages. **(J)** Chord diagram of ligand-receptor pairs in the uninfected M2-like macrophages. **(K)** Inferred ligand-receptor pairs outgoing from infected M2-like macrophages.

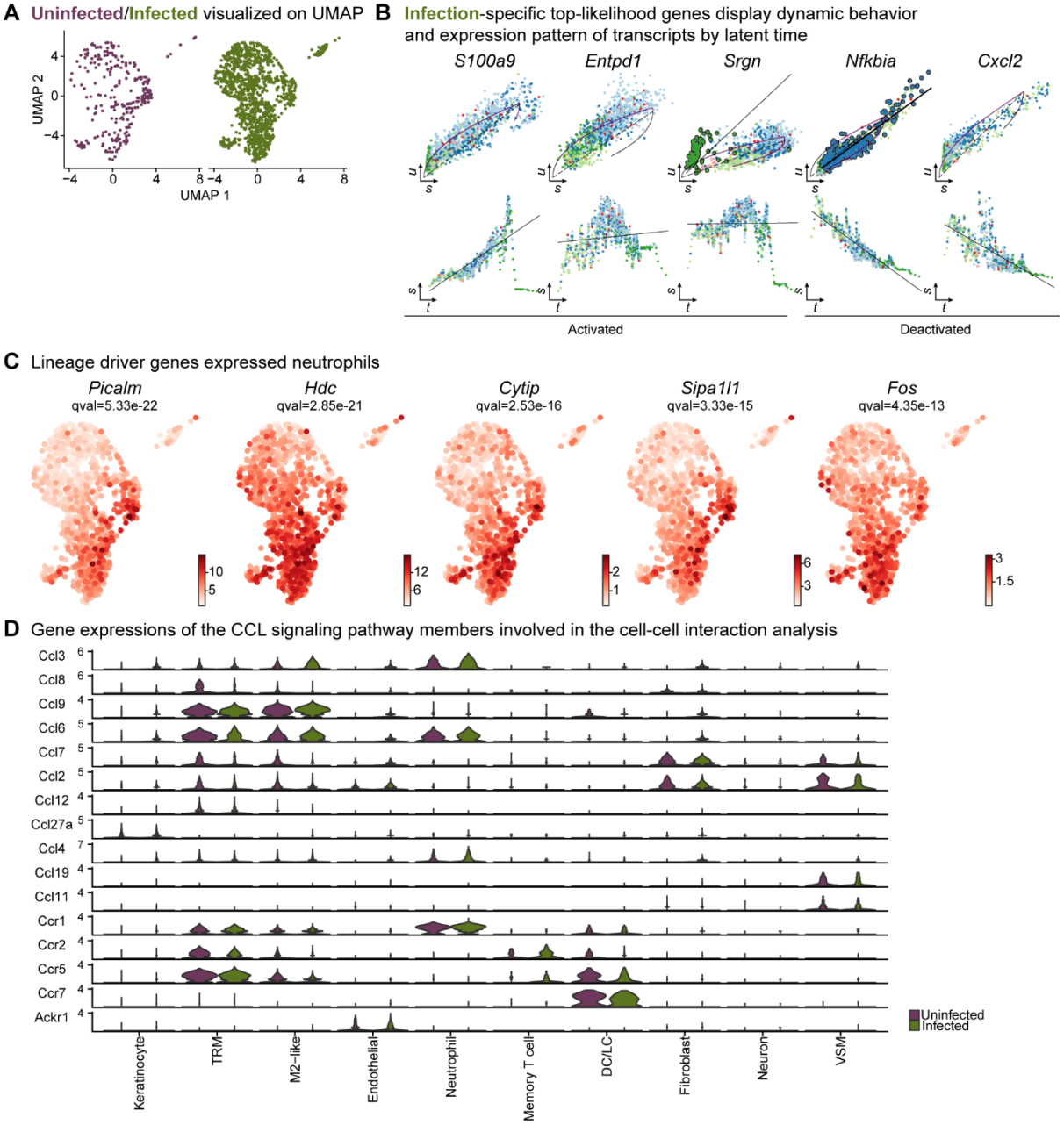

Figure S6. Neutrophil infiltration was enhanced in response to *E. faecalis* infection.
(A) UMAP representations of the extended analysis of neutrophil populations in each condition. **(B)** Infection-specific top-likelihood genes display dynamic behavior (top row) and expression pattern of transcripts by latent time (bottom row). **(C)** Lineage driver genes *Picalm*, *Hdc*, *Cytip*, *Sipa1l1,* and *Fos* were highly expressed in *Lrg1*^{hi} neutrophils. **(D)** Gene expression of the CCL signaling pathway members involved in the cell-cell interaction analysis.

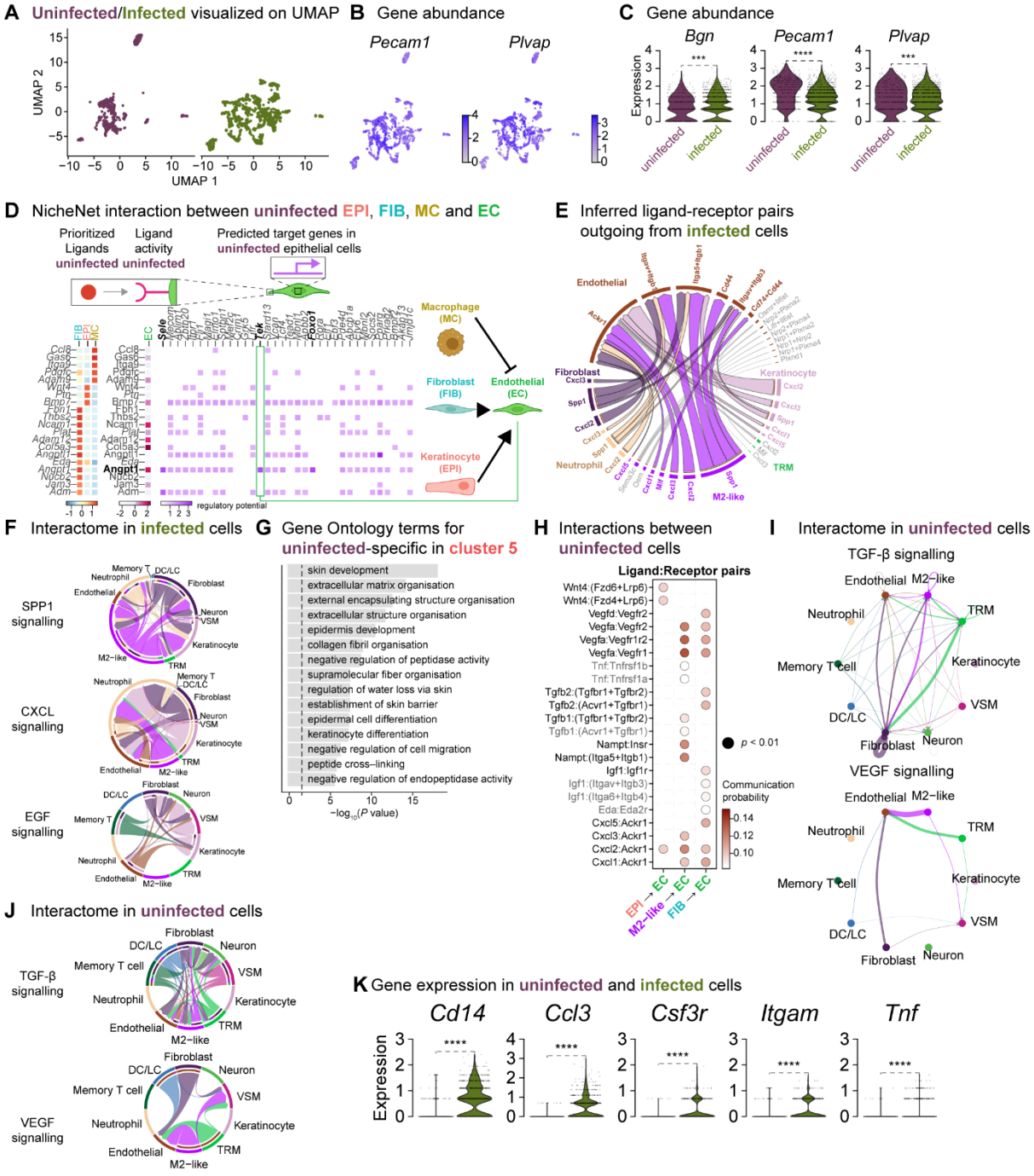

Figure S7. Fibroblasts orchestrate a reparative niche in the uninfected wounds.
(A) UMAP representations of the uninfected and infected endothelial subsets. **(B)** Spatial dispersion of endothelial cell signatures *Pecam1* and *Plvap.* **(C)** Expressions of *Bgn*, *Pecam1,* and *Plvap* in endothelial cells (Wilcoxon Rank Sum test, **** $P < 0.0001$, *** $P < 0.001$). **(D)** NicheNet interaction heat map between keratinocytes, fibroblasts, macrophages, and endothelial cells. Note the specific pairing of the fibroblast ligand angiopoietin 1 (*Angpt1*) with the TEK tyrosine receptor (*Tek*) in the uninfected niche. **(E)** Chord diagram of the cellular interactome between keratinocytes, fibroblasts, macrophages, and endothelial cells from infected populations. **(F)** Chord diagrams of the cellular interactome for TNF, SPP1 and CXCL signaling pathways across all cell types in infection. **(G)** Gene Ontology analysis of the uninfected specific ECs. **(H)** Dot plot of ligand:receptor pairs in the healing niche. **(I)** Differential interaction strengths of the cellular interactome for TGF-β and VEGF signaling pathways in the unwounded niche. **(J)** Chord diagrams of the cellular interactome for TGF-β and VEGF signaling pathways in the uninfected niche. **(K)** Infection-specific expression of *Cd14*, *Ccl3*, *Csf3r*, *Itgam,* and *Tnf* in endothelial cells (Wilcoxon Rank Sum test, **** $P < 0.0001$).

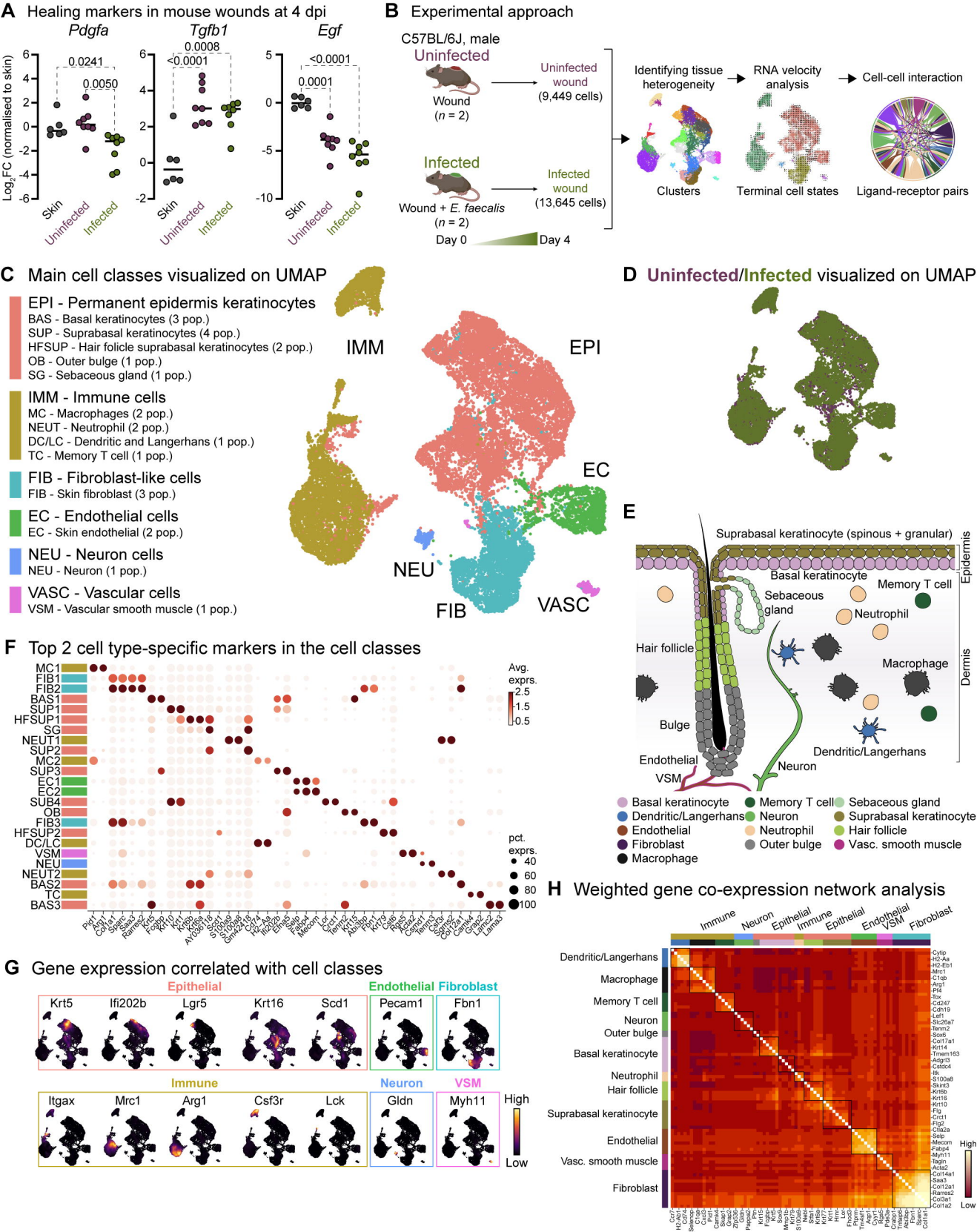
A Healing markers in mouse wounds at 4 dpi
Pdgfa
Tgfb1
Egf
Log2FC (normalised to skin)
0.0241
0.0050
0.0008
<0.0001
<0.0001
0.0001
Skin
Uninfected
Infected
B Experimental approach
C57BL/6J, male
Uninfected
Wound
(n = 2)
Uninfected wound
(9,449 cells)
Infected
Wound + E. faecalis
(n = 2)
Infected wound
(13,645 cells)
Day 0
Day 4
Identifying tissue heterogeneity
RNA velocity analysis
Cell-cell interaction
Clusters
Terminal cell states
Ligand-receptor pairs
C Main cell classes visualized on UMAP
EPI - Permanent epidermis keratinocytes
BAS - Basal keratinocytes (3 pop.)
SUP - Suprabasal keratinocytes (4 pop.)
HFSUP - Hair folicle suprabasal keratinocytes (2 pop.)
OB - Outer bulge (1 pop.)
SG - Sebaceous gland (1 pop.)
IMM - Immune cells
MC - Macrophages (2 pop.)
NEUT - Neutrophil (2 pop.)
DC/LC - Dendritic and Langerhans (1 pop.)
TC - Memory T cell (1 pop.)
FIB - Fibroblast-like cells
FIB - Skin fibroblast (3 pop.)
EC - Endothelial cells
EC - Skin endothelial (2 pop.)
NEU - Neuron cells
NEU - Neuron (1 pop.)
VASC - Vascular cells
VSM - Vascular smooth muscle (1 pop.)
IMM
EPI
EC
NEU
FIB
VASC
D Uninfected/Infected visualized on UMAP
E
Suprabasal keratinocyte (spinous + granular)
Epidermis
Dermis
Basal keratinocyte
Memory T cell
Sebaceous gland
Neutrophil
Hair follicle
Macrophage
Bulge
Dendritic/Langerhans
Endothelial
Neuron
VSM
Basal keratinocyte
Memory T cell
Sebaceous gland
Dendritic/Langerhans
Neuron
Suprabasal keratinocyte
Endothelial
Neutrophil
Hair follicle
Fibroblast
Outer bulge
Vasc. smooth muscle
Macrophage
F Top 2 cell type-specific markers in the cell classes
Avg. exprs.
pct. exprs.
G Gene expression correlated with cell classes
Epithelial
Endothelial
Fibroblast
Immune
Neuron
VSM
Krt5
Ifi202b
Lgr5
Krt16
Scd1
Pecam1
Fbn1
Itgax
Mrc1
Arg1
Csf3r
Lck
Gldn
Myh11
High
Low
H Weighted gene co-expression network analysis
Immune
Neuron
Epithelial
Immune
Epithelial
Endothelial
VSM
Fibroblast
Dendritic/Langerhans
Macrophage
Memory T cell
Neuron
Outer bulge
Basal keratinocyte
Neutrophil
Hair follicle
Suprabasal keratinocyte
Endothelial
Vasc. smooth muscle
Fibroblast
High
Low

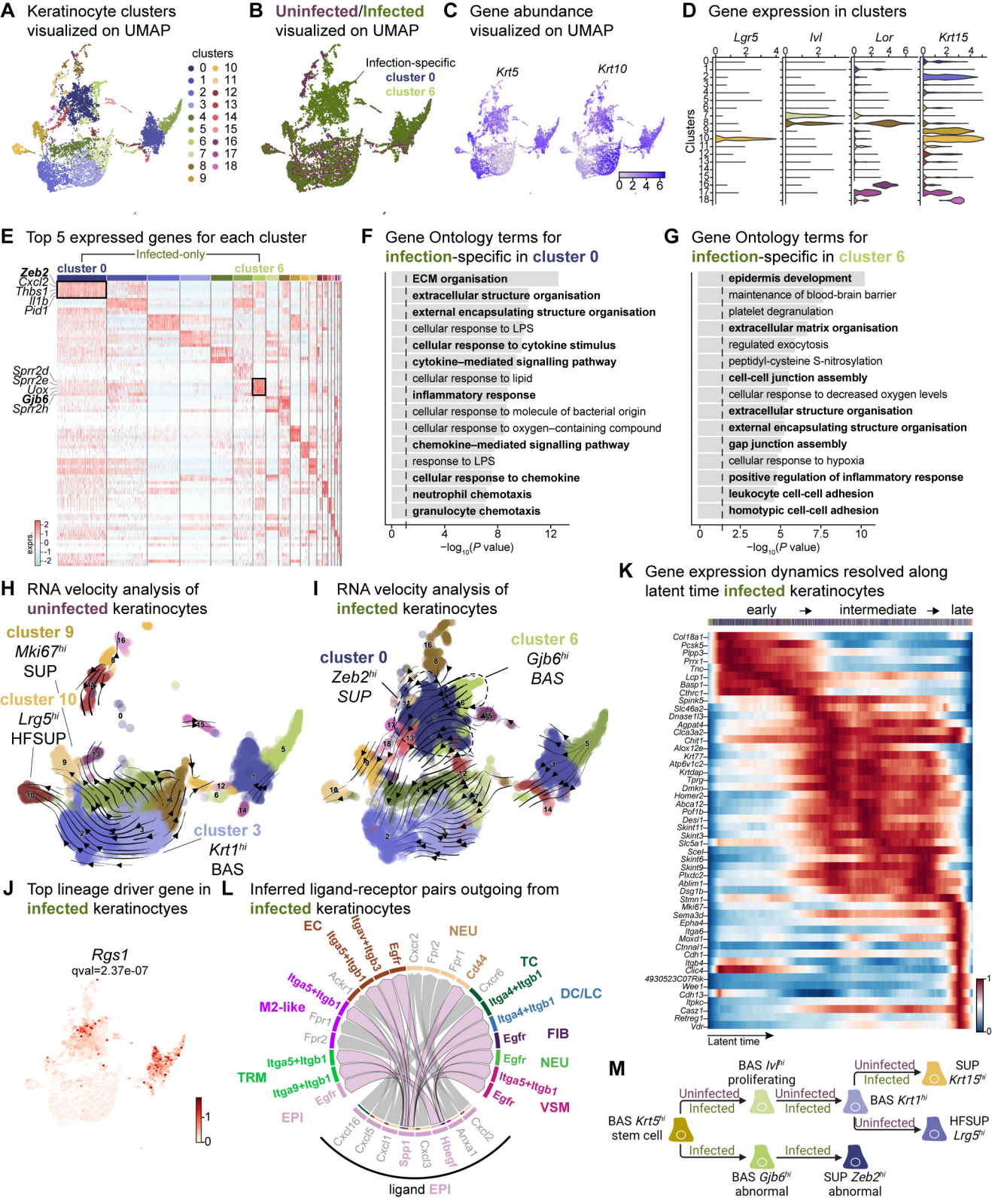
A Keratinocyte clusters visualized on UMAP
clusters
0 1 2 3 4 5 6 7 8 9 10 11 12 13 14 15 16 17 18
B Uninfected/Infected visualized on UMAP
Infection-specific
cluster 0
cluster 6
C Gene abundance visualized on UMAP
Krt5
Krt10
0 2 4 6
D Gene expression in clusters
Lgr5
Ivl
Lor
Krt15
Clusters
E Top 5 expressed genes for each cluster
Infected-only
cluster 0
cluster 6
Zeb2
Cxcl2
Thbs1
Il1b
Pid1
Sprr2d
Sprr2e
Lcn
Gjb6
Sprr2h
exprs
F Gene Ontology terms for infection-specific in cluster 0
ECM organisation
extracellular structure organisation
external encapsulating structure organisation
cellular response to LPS
cellular response to cytokine stimulus
cytokine–mediated signalling pathway
cellular response to lipid
inflammatory response
cellular response to molecule of bacterial origin
cellular response to oxygen–containing compound
chemokine–mediated signalling pathway
response to LPS
cellular response to chemokine
neutrophil chemotaxis
granulocyte chemotaxis
−log10(P value)
G Gene Ontology terms for infection-specific in cluster 6
epidermis development
maintenance of blood-brain barrier
platelet degranulation
extracellular matrix organisation
regulated exocytosis
peptidyl-cysteine S-nitrosylation
cell-cell junction assembly
cellular response to decreased oxygen levels
extracellular structure organisation
external encapsulating structure organisation
gap junction assembly
cellular response to hypoxia
positive regulation of inflammatory response
leukocyte cell-cell adhesion
homotypic cell-cell adhesion
−log10(P value)
H RNA velocity analysis of uninfected keratinocytes
cluster 9
Mki67hi
SUP
cluster 10
Lrg5hi
HFSUP
cluster 3
Krt1hi
BAS
I RNA velocity analysis of infected keratinocytes
cluster 0
Zeb2hi
SUP
cluster 6
Gjb6hi
BAS
K Gene expression dynamics resolved along latent time infected keratinocytes
early
intermediate
late
Latent time
J Top lineage driver gene in infected keratinoctyes
Rgs1
qval=2.37e-07
L Inferred ligand-receptor pairs outgoing from infected keratinocytes
EC
Itga5+Itgb1
Itgav+Itgb3
Egfr
NEU
Cxcr2
Fpr2
Fpr1
Cd44
TC
Cxcr6
Itga4+Itgb1
DC/LC
Itga4+Itgb1
Egfr
FIB
Egfr
NEU
Itga5+Itgb1
Egfr
VSM
Egfr
EPI
Cxcl16
Cxcl5
Cxcl1
Spp1
Cxcl3
Hbegf
Anxa1
Cxcl2
ligand EPI
TRM
Itga5+Itgb1
Itga9+Itgb1
Egfr
M2-like
Itga5+Itgb1
Ackr1
Fpr1
Fpr2
M
BAS Ivlhi proliferating
Uninfected
Infected
Uninfected
Infected
SUP Krt15hi
BAS Krt1hi
Uninfected
HFSUP Lrg5hi
BAS Krt5hi stem cell
Infected
Infected
BAS Gjb6hi abnormal
SUP Zeb2hi abnormal

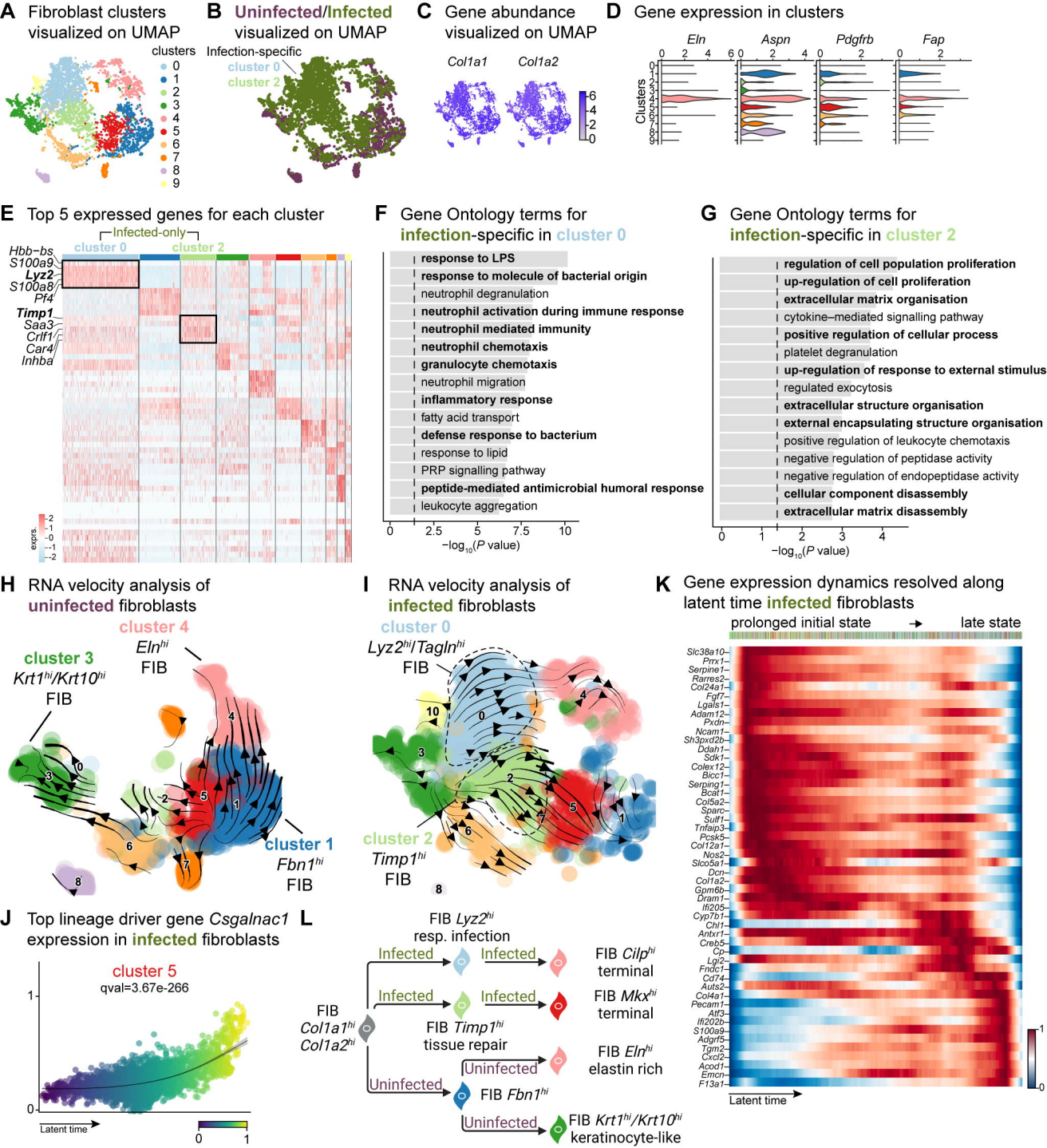
A
Fibroblast clusters visualized on UMAP
clusters
0
1
2
3
4
5
6
7
8
9
B
Uninfected/Infected visualized on UMAP
Infection-specific
cluster 0
cluster 2
C
Gene abundance visualized on UMAP
Col1a1
Col1a2
6
4
2
0
D
Gene expression in clusters
Eln
Aspn
Pdgfrb
Fap
Clusters
E
Top 5 expressed genes for each cluster
Infected-only
cluster 0
cluster 2
Hbb-bs
S100a9
Lyz2
S100a8
Pf4
Timp1
Saa3
Crlf1
Car4
Inhba
exprs.
F
Gene Ontology terms for infection-specific in cluster 0
response to LPS
response to molecule of bacterial origin
neutrophil degranulation
neutrophil activation during immune response
neutrophil mediated immunity
neutrophil chemotaxis
granulocyte chemotaxis
neutrophil migration
inflammatory response
fatty acid transport
defense response to bacterium
response to lipid
PRP signalling pathway
peptide-mediated antimicrobial humoral response
leukocyte aggregation
−log10(P value)
G
Gene Ontology terms for infection-specific in cluster 2
regulation of cell population proliferation
up-regulation of cell proliferation
extracellular matrix organisation
cytokine–mediated signalling pathway
positive regulation of cellular process
platelet degranulation
up-regulation of response to external stimulus
regulated exocytosis
extracellular structure organisation
external encapsulating structure organisation
positive regulation of leukocyte chemotaxis
negative regulation of peptidase activity
negative regulation of endopeptidase activity
cellular component disassembly
extracellular matrix disassembly
−log10(P value)
H
RNA velocity analysis of uninfected fibroblasts
cluster 4
Eln^hi FIB
cluster 3
Krt1^hi/Krt10^hi FIB
cluster 1
Fbn1^hi FIB
I
RNA velocity analysis of infected fibroblasts
cluster 0
Lyz2^hi/Tagln^hi FIB
cluster 2
Timp1^hi FIB
K
Gene expression dynamics resolved along latent time infected fibroblasts
prolonged initial state
late state
Latent time
J
Top lineage driver gene Csgalnac1 expression in infected fibroblasts
cluster 5
qval=3.67e-266
Latent time
L
FIB Lyz2^hi resp. infection
Infected
Infected
FIB Cilp^hi terminal
Infected
Infected
FIB Mkx^hi terminal
FIB Col1a1^hi Col1a2^hi
FIB Timp1^hi tissue repair
FIB Eln^hi elastin rich
Uninfected
Uninfected
FIB Fbn1^hi
Uninfected
FIB Krt1^hi/Krt10^hi keratinocyte-like

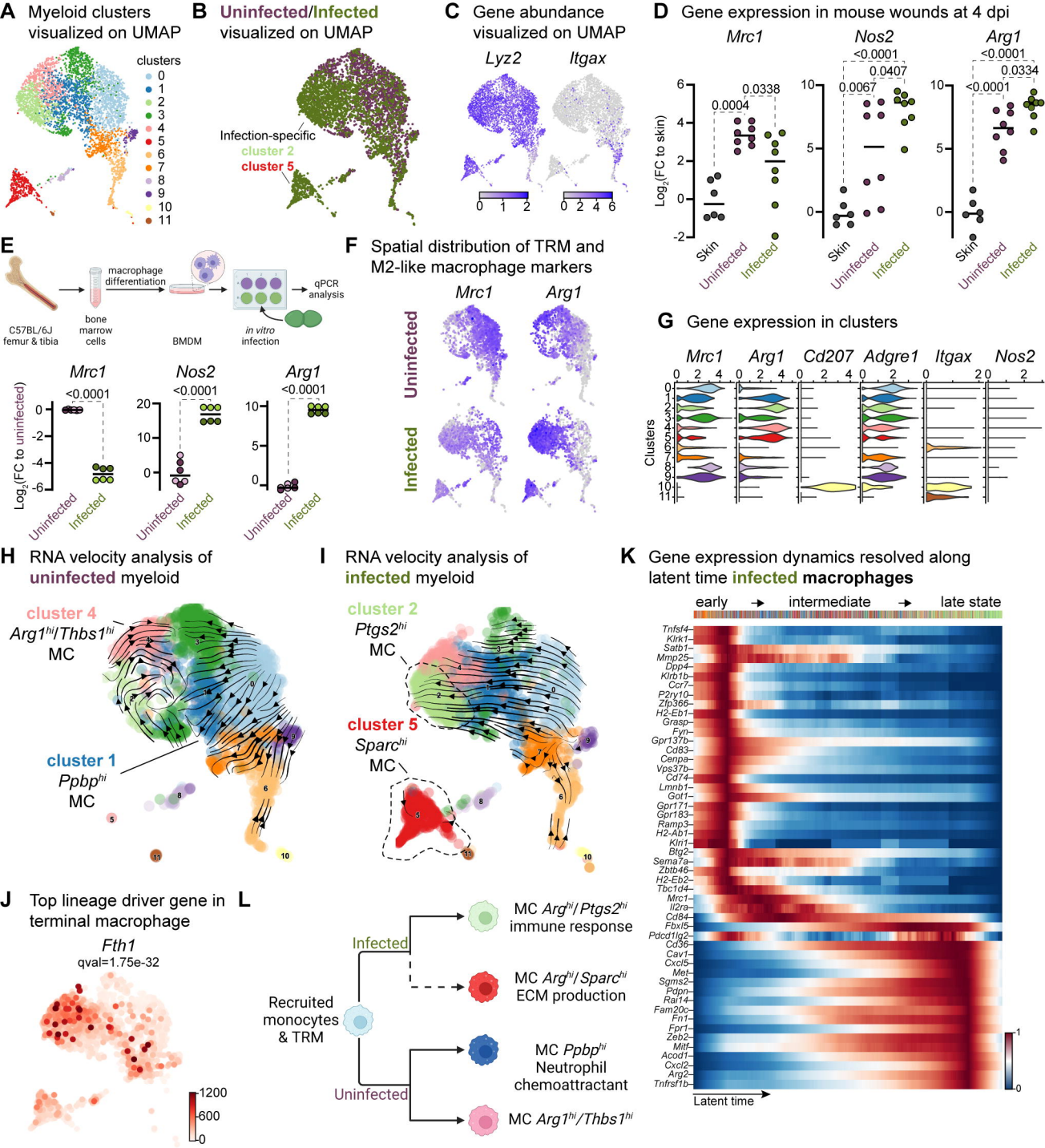
A
Myeloid clusters visualized on UMAP
clusters
0
1
2
3
4
5
6
7
8
9
10
11
B
Uninfected/Infected visualized on UMAP
Infection-specific
cluster 2
cluster 5
C
Gene abundance visualized on UMAP
Lyz2
Itgax
0 1 2
0 2 4 6
D
Gene expression in mouse wounds at 4 dpi
Mrc1
Nos2
Arg1
Log2(FC to skin)
0.0004
0.0338
<0.0001
0.0067
0.0407
<0.0001
<0.0001
0.0334
Skin
Uninfected
Infected
E
macrophage differentiation
C57BL/6J femur & tibia
bone marrow cells
BMDM
in vitro infection
qPCR analysis
Mrc1
Nos2
Arg1
<0.0001
Log2(FC to uninfected)
Uninfected
Infected
F
Spatial distribution of TRM and M2-like macrophage markers
Mrc1
Arg1
Uninfected
Infected
G
Gene expression in clusters
Mrc1
Arg1
Cd207
Adgre1
Itgax
Nos2
Clusters
H
RNA velocity analysis of uninfected myeloid
cluster 4
Arg1hi/Thbs1hi MC
cluster 1
Ppbphi MC
I
RNA velocity analysis of infected myeloid
cluster 2
Ptgs2hi MC
cluster 5
Sparchi MC
K
Gene expression dynamics resolved along latent time infected macrophages
early
intermediate
late state
Tnfsf4
Klrk1
Satb1
Mmp25
Dpp4
Klrb1b
Ccr7
P2ry10
Zfp366
H2-Eb1
Grasp
Fyn
Gpr137b
Cd63
Cenpa
Vps37b
Cd74
Lmnb1
Golt1
Gpr171
Gpr183
Ramp3
H2-Ab1
Klrc1
Btg2
Sema7a
Zbtb46
H2-Eb2
Tbc1d4
Mrc1
Il2ra
Cd84
Fbxl5
Pdcd1lg2
Cd36
Cavl
Cxcl5
Met
Sgms2
Pdpn
Ral14
Fam20c
Fn1
Fpr1
Zeb2
Mitf
Acod1
Cxcl2
Arg2
Tnfrsf1b
Latent time
J
Top lineage driver gene in terminal macrophage
Fth1
qval=1.75e-32
1200
600
0
L
Recruited monocytes & TRM
Infected
Uninfected
MC Arghi/Ptgs2hi immune response
MC Arghi/Sparchi ECM production
MC Ppbphi Neutrophil chemoattractant
MC Arg1hi/Thbs1hi

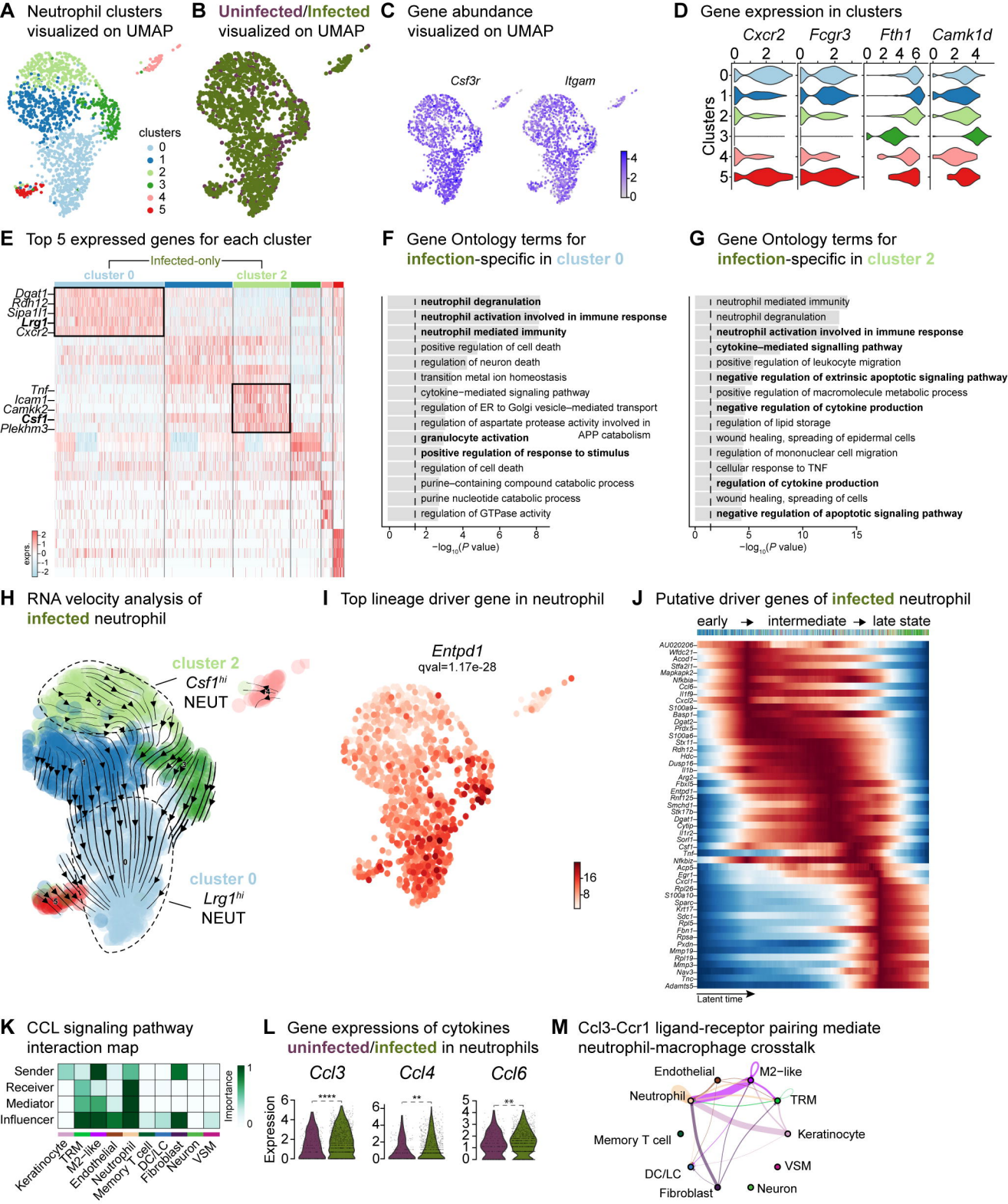
A Neutrophil clusters visualized on UMAP
clusters
0
1
2
3
4
5
B Uninfected/Infected visualized on UMAP
C Gene abundance visualized on UMAP
Csf3r
Itgam
4
2
0
D Gene expression in clusters
Cxcr2
Fcgr3
Fth1
Camk1d
Clusters
E Top 5 expressed genes for each cluster
Infected-only
cluster 0
cluster 2
Dgat1
Rdh12
Sipa1l1
Lrg1
Cxcr2
Tnf
Icam1
Camkk2
Csf1
Plekhm3
exprs.
F Gene Ontology terms for infection-specific in cluster 0
neutrophil degranulation
neutrophil activation involved in immune response
neutrophil mediated immunity
positive regulation of cell death
regulation of neuron death
transition metal ion homeostasis
cytokine−mediated signaling pathway
regulation of ER to Golgi vesicle−mediated transport
regulation of aspartate protease activity involved in APP catabolism
granulocyte activation
positive regulation of response to stimulus
regulation of cell death
purine−containing compound catabolic process
purine nucleotide catabolic process
regulation of GTPase activity
−log10(P value)
G Gene Ontology terms for infection-specific in cluster 2
neutrophil mediated immunity
neutrophil degranulation
neutrophil activation involved in immune response
cytokine−mediated signalling pathway
positive regulation of leukocyte migration
negative regulation of extrinsic apoptotic signaling pathway
positive regulation of macromolecule metabolic process
negative regulation of cytokine production
regulation of lipid storage
wound healing, spreading of epidermal cells
regulation of mononuclear cell migration
cellular response to TNF
regulation of cytokine production
wound healing, spreading of cells
negative regulation of apoptotic signaling pathway
−log10(P value)
H RNA velocity analysis of infected neutrophil
cluster 2
Csf1hi
NEUT
cluster 0
Lrg1hi
NEUT
I Top lineage driver gene in neutrophil
Entpd1
qval=1.17e-28
16
8
J Putative driver genes of infected neutrophil
early
intermediate
late state
Latent time
K CCL signaling pathway interaction map
Sender
Receiver
Mediator
Influencer
Importance
Keratinocyte
TRM
M2−like
Endothelial
Neutrophil
Memory T cell
DC/LC
Fibroblast
Neuron
VSM
L Gene expressions of cytokines uninfected/infected in neutrophils
Ccl3
Ccl4
Ccl6
Expression
M Ccl3-Ccr1 ligand-receptor pairing mediate neutrophil-macrophage crosstalk
Endothelial
M2−like
Neutrophil
TRM
Memory T cell
Keratinocyte
DC/LC
VSM
Fibroblast
Neuron

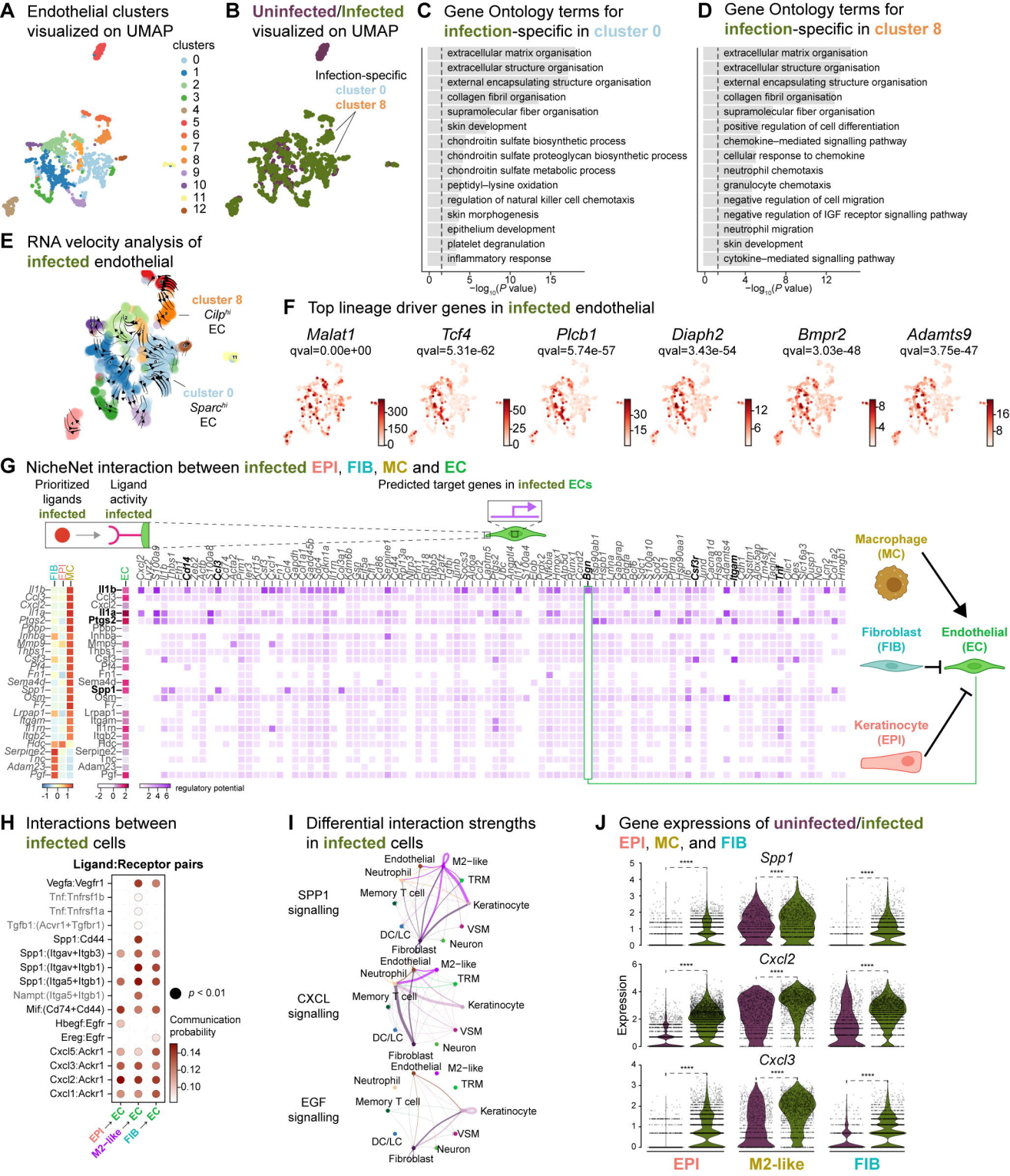
A Endothelial clusters visualized on UMAP
clusters
0
1
2
3
4
5
6
7
8
9
10
11
12
B Uninfected/Infected visualized on UMAP
Infection-specific
cluster 0
cluster 8
C Gene Ontology terms for infection-specific in cluster 0
extracellular matrix organisation
extracellular structure organisation
external encapsulating structure organisation
collagen fibril organisation
supramolecular fiber organisation
skin development
chondroitin sulfate biosynthetic process
chondroitin sulfate proteoglycan biosynthetic process
chondroitin sulfate metabolic process
peptidyl–lysine oxidation
regulation of natural killer cell chemotaxis
skin morphogenesis
epithelium development
platelet degranulation
inflammatory response
0
5
10
15
−log10(P value)
D Gene Ontology terms for infection-specific in cluster 8
extracellular matrix organisation
extracellular structure organisation
external encapsulating structure organisation
collagen fibril organisation
supramolecular fiber organisation
positive regulation of cell differentiation
chemokine–mediated signalling pathway
cellular response to chemokine
neutrophil chemotaxis
granulocyte chemotaxis
negative regulation of cell migration
negative regulation of IGF receptor signalling pathway
neutrophil migration
skin development
cytokine–mediated signalling pathway
0
4
8
12
−log10(P value)
E RNA velocity analysis of infected endothelial
cluster 8
Cilphi
EC
culster 0
Sparchi
EC
F Top lineage driver genes in infected endothelial
Malat1
qval=0.00e+00
Tcf4
qval=5.31e-62
Plcb1
qval=5.74e-57
Diaph2
qval=3.43e-54
Bmpr2
qval=3.03e-48
Adamts9
qval=3.75e-47
G NicheNet interaction between infected EPI, FIB, MC and EC
Prioritized ligands infected
Ligand activity infected
Predicted target genes in infected ECs
FIB
EPI
MC
EC
Il1b
Ccl3
Cxcl2
Il1a
Ptgs2
Pbpp
Inhba
Mmp9
Thbs1
Csf3
Pf4
Fn1
Sema4d
Spp1
Osm
F7
Lrpap1
Itgam
Il1rn
Itgb2
Hdc
Serpine2
Tnc
Adam23
Pgf
regulatory potential
Macrophage (MC)
Fibroblast (FIB)
Endothelial (EC)
Keratinocyte (EPI)
H Interactions between infected cells
Ligand:Receptor pairs
Vegfa:Vegfr1
Tnf:Tnfrsf1b
Tnf:Tnfrsf1a
Tgfb1:(Acvr1+Tgfbr1)
Spp1:Cd44
Spp1:(Itgav+Itgb3)
Spp1:(Itgav+Itgb1)
Spp1:(Itga5+Itgb1)
Nampt:(Itga5+Itgb1)
Mif:(Cd74+Cd44)
Hbegf:Egfr
Ereg:Egfr
Cxcl5:Ackr1
Cxcl3:Ackr1
Cxcl2:Ackr1
Cxcl1:Ackr1
p < 0.01
Communication probability
0.14
0.12
0.10
EPI → EC
M2-like → EC
FIB → EC
I Differential interaction strengths in infected cells
SPP1 signalling
CXCL signalling
EGF signalling
Endothelial
M2−like
Neutrophil
TRM
Memory T cell
Keratinocyte
VSM
DC/LC
Neuron
Fibroblast
J Gene expressions of uninfected/infected EPI, MC, and FIB
Spp1
Cxcl2
Cxcl3
Expression
EPI
M2-like
FIB